Characterization of MEMS Electrostatic Actuators Beyond Pull-In

A Thesis
Submitted for the Degree of
Master of Science (Engineering)
in Faculty of Engineering

by

Gorthi V.R.M.S. Subrahmanyam

Supercomputer Education and Research Centre
Indian Institute of Science
Bangalore – 560 012 (INDIA)

January 2006

Acknowledgments

I would like to express my immense gratitude to my adviser Dr. Atanu Mohanty, who supported me greatly and did every possible effort to teach and help me. I am more than thankful to him for patiently educating me. He is probably the best teacher I have ever come across. He gave complete freedom and helped me in all aspects. I am very happy to be blessed with such a care taking, friendly and knowledgeable guide.

I am indebted to Dr. Anindya Chatterjee for his guidance and parental care. He guided in many aspects of this work particularly, the chapter on dynamic analysis is a result of his guidance. The interactions with him are very informative and pleasant memories for ever. I am inspired by his attitude, workaholic nature and concern for others. Most of my learning in IISc is from these two teachers.

I would like to thank Prof. S. K. Sen for his encouragement. I am thankful to Dr. Sayanu for the lectures on MEMS and introducing some of the basic concepts of MEMS. The discussions that I had with him are very helpful. I wish to thank Dr. K. J. Vinoy for the useful course work on Antennas and MEMS. He is always very kind and helpful to me. I am thankful to Dr. G. K. Ananthasuresh for allowing me to attend his course on MEMS and also for going through the manuscript of the paper patiently and making suggestions. I thank Dr. Raha for teaching me data structures. Thanks are due to the Chairman of our department for his support. I am thankful to my friends Prasad, Rajan, Surya, Rupesh, Ashok, Rahul, Jay, Sangamesh, Vivek and many others. I would like thank all the staff of SERC for their friendliness and cooperation. Thanks to all the people who are involved in the development of Linux, Latex, LyX, and Dia.

Last but not the least, I am indebted to my parents, sisters: Lalitha, Radha, and my

brother: Sai Siva. The care, love and affection of them are responsible for my present stage. I am thankful to the God for pouring His love through all these people.

All these things became possible in my life only because of the inspiration, guidance and support of Sri P. Subbaramaih sir of Golagamudi, I would like to express my heart-felt gratitude to Sri Subbaramaih Sir. Finally and most importantly, I offer my pranamas to the lotus feet of Sri Ekkirala Bharadwaja master, Sai Baba of Shirdi, and Bhagavan Sri Venkaiah Swamy of Golagamudi.

Abstract

The operational range of MEMS electrostatic parallel plate actuators can be extended beyond pull-in with the presence of an intermediate dielectric layer, which has a significant effect on the behaviour of such actuators. Here we study the behaviour of cantilever beam electrostatic actuators beyond pull-in using a beam model along with a dielectric layer. Three possible static configurations of the beam are identified over the operational voltage range. We call them floating, pinned and flat: the latter two are also called arc-type and S-type in the literature. We compute the voltage ranges over which the three configurations can exist, and the points where transitions occur between these configurations. Voltage ranges are identified where bi-stable and tri-stable states exist. A classification of all possible transitions (pull-in and pull-out as well as transitions we term pull-down and pull-up) is presented based on the dielectric layer parameters. A scaling law is found in the flat configuration. Dynamic stability analyses are presented for the floating and pinned configurations. For high dielectric layer thickness, discontinuous transitions between configurations disappear and the actuator has smooth predictable behaviour, but at the expense of lower tunability. Hence, designs with variable dielectric layer thickness can be studied in future to obtain both regularity/predictability as well as high tunability.

Contents

Abstract iii

Publications based on this Thesis ix

1 Introduction 1
- 1.1 Background and Motivation . . . 1
- 1.2 MEMS Parallel Plate Electrostatic Actuators . . . 3
  - 1.2.1 Simple Lumped-Element Model . . . 3
  - 1.2.2 Pull-in Voltage . . . 4
  - 1.2.3 Deflection . . . 5
  - 1.2.4 Applications . . . 7
  - 1.2.5 Limitations of Lumped Model . . . 10
- 1.3 Thesis Organization . . . 10

2 Mathematical Modeling and Simulations 12
- 2.1 Introduction . . . 12
- 2.2 Possible Configurations . . . 12
- 2.3 Governing Equation . . . 14
- 2.4 Normalized Equation . . . 15
- 2.5 Modal Expansion Method . . . 17
  - 2.5.1 Modal Expansion Method in General . . . 17
  - 2.5.2 Floating Configuration . . . 20
  - 2.5.3 Pinned Configuration . . . 22
  - 2.5.4 Procedure to Solve the Coupled Equation . . . 24
  - 2.5.5 Modified Procedure using Newton's Method . . . 25
- 2.6 Finite Difference Approximation . . . 31
  - 2.6.1 Method . . . 31
  - 2.6.2 Floating Configuration . . . 33
  - 2.6.3 Pinned Configuration . . . 34
  - 2.6.4 Flat Configuration . . . 36
- 2.7 Scaling Law in the Flat Configuration . . . 37
- 2.8 Discussion and Conclusions . . . 38

3 Effects of Dielectric Layer **40**
3.1 Introduction . . . 40
3.2 Normalized Voltage (V) Limits of Configurations . . . 40
3.3 Transitions . . . 41
3.3.1 Pull-In . . . 43
3.3.2 Pull-Down . . . 44
3.3.3 Pull-Up . . . 44
3.3.4 Pull-out . . . 45
3.4 Bi-stability . . . 45
3.5 Discussion and Conclusions . . . 46

4 Dynamic Stability of Equilibrium Solutions **48**
4.1 Introduction . . . 48
4.2 Method . . . 48
4.3 Stability Results . . . 52
4.4 Discussion and Conclusions . . . 53

5 Case Study **55**

6 Conclusions and Further Work **61**

Bibliography **62**

List of Tables

2.1 Boundary conditions at the free end of the cantilever beam for the three configurations. 14
2.2 Description of the parameters in the governing equation. 15
2.3 Roots and coefficient values of various modes of the floating configuration. 21
2.4 Roots and coefficient values of various modes of the pinned configuration. . 23
2.5 Characteristic equations, coefficient values and Initial position of the beam for various configurations. 24

5.1 Dimensions and material properties of a MEMS actuator. 55

List of Figures

1.1 Simple lumped-element model of MEMS electrostatic parallel plate actuator with 1 degree of freedom . . . 3
1.2 Solutions of MEMS electrostatic actuator without dielectric layer . . . 7
1.3 Solutions of MEMS electrostatic actuator for different dielectric layer thickness values . . . 8
1.4 C-V characteristics of MEMS electrostatic actuator for different dielectric layer thickness values . . . 9

2.1 Schematic view of the cantilever beam electrostatic actuator. . . . 13
2.2 Possible configurations of the cantilever beam actuator. (The scale in the vertical direction is exaggerated.) . . . 14
2.3 Flow chart for Modal Expansion Method. . . . 26
2.4 Flow chart for Modal Expansion Method that employs Newton's Method. . . 30
2.5 Flow chart for Finite difference approximation of floating and pinned configurations. . . . 35

3.1 V limits of the three configurations. . . . 42
3.2 Classification of possible transitions based on the numerical results of Fig. 3.1. 42
3.3 Variation of the magnitude of the pull-in discontinuity with h. . . . 43
3.4 Pull-down: jump in slope at the touching end of the beam. . . . 44
3.5 Variation of the magnitude of the pull-down discontinuity with h. . . . 45
3.6 Variation of width of bi-stability region with h. . . . 46

4.1 Stability analysis of the floating configuration. . . . 52
4.2 Stability analysis of the pinned configuration. . . . 53

5.1 Floating configuration: Variation of height at the free end of the beam with applied voltage. . . . 56
5.2 Pinned configuration: Contact force at the touching end of the beam vs. applied voltage. . . . 57
5.3 Pinned configuration: Slope at the contact point of the cantilever beam vs. applied voltage. . . . 58
5.4 Flat configuration: Contact length of the cantilever beam with the dielectric layer vs. applied voltage. . . . 59
5.5 Voltage ranges of the three configurations. . . . 59

5.6 C-V characteristics in the floating configuration. 60
5.7 C-V characteristics in the flat configuration. 60

6.1 Proposed designs to achieve more regular and reversible behaviour as well as higher tunability 61

Publications based on this Thesis

- **Subrahmanyam Gorthi**, Atanu Mohanty and Anindya Chatterjee, "Cantilever beam electrostatic MEMS actuators beyond pull-in," in *Journal of Micromechanics and MicroEngineering*, vol. 16, num. 9, 1800-1810, 2006.

- **Subrahmanyam Gorthi**, Atanu Mohanty and Anindya Chatterjee, "MEMS parallel plate actuators: pull-in, pull-out and other transitions," presented in *International Conference on MEMS and Semiconductor Nanotechnology*, December 20-22, IIT Kharagpur, India.

Chapter 1

Introduction

This thesis presents a study of cantilever beam MEMS electrostatic actuators beyond pull-in. The effects are studied of an intermediate dielectric layer on the possible configurations of the actuator and transitions between them.

1.1 Background and Motivation

MEMS (Micro-Electro-Mechanical-Systems) are the microscopic structures integrated onto silicon (or similar substrate) that combine mechanical, optical, fluidic and other elements with electronics. These devices enable the realization of complete system-on-a-chip. MEMS make it possible for systems to be smaller, faster, more energy efficient, more functional and less expensive. In a typical MEMS configuration, integrated circuits (ICs) provide the "thinking part" of the system, while MEMS complement this intelligence with active perception and control functions.

Electrostatic actuation is one of the most commonly used schemes for MEMS devices. In MEMS electrostatic parallel plate actuators (discussed in detail in the next section), the moving plate comes to equilibrium when the electrostatic force is balanced by the restoring mechanical force. The restoring force increases (approximately) linearly with deflection whereas the electrostatic force is inversely proportional to the square of the distance between the plates. Due to this nonlinear nature of the electrostatic force, as

the moving plate traverses about one third of the total distance between the plates, the restoring force can no longer be able to balance the electrostatic force and hence, the moving plate (electrode) flaps onto the other plate. This is known as *pull-in phenomena* and the corresponding voltage is called *pull-in voltage*.

Thus the operational range of MEMS electrostatic parallel plate actuators is limited by the pull-in phenomena. The behaviour of the MEMS actuators before pull-in is studied extensively in the literature [1–11]. With the presence of an intermediate dielectric layer between the electrodes, the operational range can be extended beyond the pull-in and they can be meaningfully modeled over the entire operational range. Many MEMS devices operate beyond pull-in, e.g. capacitive switches [12, 13], zipper varactors [14, 15] and CPW resonators [16]. However, the behaviour of MEMS devices beyond the pull-in has not been studied in greater detail in the literature. This thesis presents a detailed analysis of the cantilever beam MEMS electrostatic actuators, particularly beyond the pull-in. The effects of an intermediate dielectric layer are also studied in detail and a frame work of all possible types of transitions between the configuration is made based on the dielectric layer thickness.

Simple lumped element models of MEMS actuators with a single degree of freedom [17–20] result in easy calculations but fail to capture details of the behaviour beyond the pull-in. At the other end of modeling complexities, simulations of MEMS actuators beyond the pull-in have been done using 3-D models [21]. Similar approaches have been used in studying the hysteresis characteristics of electrostatic actuators [22]. 3-D models [2,21,22] lead to a detailed and accurate prediction, but simulations are expensive in time and computation, particularly for problems involving mechanical contacts. In this thesis, we employ a 1-D analysis that, at an intermediate level of complexity, gives useful results with reasonable effort. Note that existing comparisons between 1-D and more detailed models show that 1-D analysis can in fact provide useful results and insights [23, 24].

The following section provides an introduction to MEMS electrostatic parallel plate actuators with an intermediate dielectric layer between the electrodes, using a simple lumped element spring-mass-damper model.

1.2 MEMS Parallel Plate Electrostatic Actuators

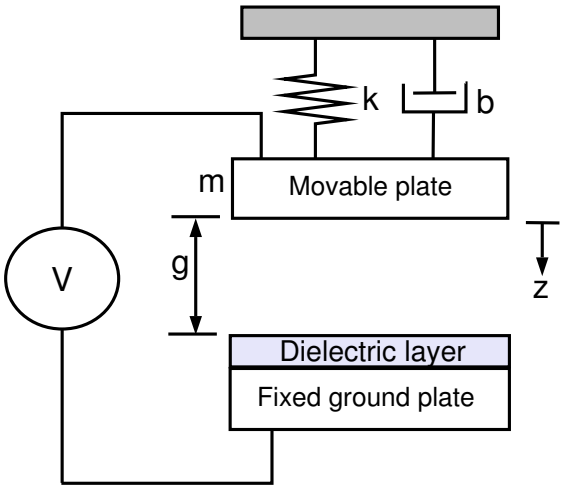

Figure 1.1: Simple lumped-element model of MEMS electrostatic parallel plate actuator with 1 degree of freedom

MEMS parallel plate actuators typically consist of a fixed bottom plate and an upper plate fixed at either one end or two ends. Actuators with one end of the upper electrode fixed and the other end being free to move are called cantilever beam actuators and the actuators with two ends of the upper electrode fixed are called fixed-fixed beam actuators.

1.2.1 Simple Lumped-Element Model

Fig. 1.1 shows the simple lumped element model of the MEMS electrostatic parallel plate actuators with one degree of freedom. The actuator has an intermediate dielectric layer deposited over the bottom electrode. The quantities m, k, b in the figure represent the mass, spring constant and damping coefficient respectively; g is the initial gap between the electrodes; t_d and ϵ_r are the dielectric thickness and relative permittivity of the dielectric layer respectively.

The equation governing the deflection of the moving electrode shown Fig. 1.1 is [6]

$$m\,\frac{d^2z}{dt^2} + b\,\frac{dz}{dt} + k\,z = F_e \tag{1.1}$$

where F_e is the electrostatic force and is derived as follows. The capacitance of the

electrostatic actuator is

$$C = \frac{\epsilon_0 A}{g - z + \frac{t_d}{\epsilon_r}} \tag{1.2}$$

where A is area of the plate and ϵ_0 is permittivity of free space. The effect of fringing is not considered throughout in order to simplify the analysis. The electrical energy stored in the parallel plate actuator is

$$E = \frac{1}{2} C V^2 = \frac{\epsilon_0 A V^2}{2 \left(g - z + \frac{t_d}{\epsilon_r}\right)}. \tag{1.3}$$

The electrostatic force is

$$F_e = \frac{dE}{dz} = \frac{\epsilon_0 A V^2}{2 \left(g - z + \frac{t_d}{\epsilon_r}\right)^2}. \tag{1.4}$$

Substituting F_e in Eq. 1.1,

$$m \frac{d^2 z}{dt^2} + b \frac{dz}{dt} + k z = \frac{\epsilon_0 A V^2}{2 \left(g - z + \frac{t_d}{\epsilon_r}\right)^2}. \tag{1.5}$$

When a DC potential is applied across the electrodes, at steady state, the above equation reduces to

$$k z = \frac{\epsilon_0 A V^2}{2 \left(g - z + \frac{t_d}{\epsilon_r}\right)^2}. \tag{1.6}$$

Note that the mechanical restoring force is given by the term on the left side of the above equation and it varies linearly with deflection whereas the electrostatic force is given by the right side term and is inversely proportional to the square of the deflection.

1.2.2 Pull-in Voltage

The expression for voltage, derived from Eq. 1.6 is

$$V = \sqrt{\frac{2k}{\epsilon_0 A} z \left(g - z + \frac{t_d}{\epsilon_r}\right)^2}. \tag{1.7}$$

Pull-in corresponds to the voltage at which maximum deflection occurs. Hence, by taking the derivative of Eq. 1.7 with respect to deflection and equating it to zero, we get

$$z = \frac{1}{3}\left(g + \frac{t_d}{\epsilon_r}\right). \tag{1.8}$$

The pull-in voltage is computed by substituting the the above value in Eq. 1.7 and is given by

$$V_{pull-in} = \sqrt{\frac{8\,k}{27\,\epsilon_0\,A}\,\left(g + \frac{t_d}{\epsilon_r}\right)^3}. \tag{1.9}$$

The following observations can be made from the Eq. 1.8 & 1.9.

1. When there is no dielectric layer ($t_d = 0$), pull-in occurs as the electrode traverses one third of the initial gap.

2. With the increase in dielectric layer thickness, the electrode can smoothly traverse over larger distances. For $\frac{t_d}{\epsilon_r} \geq 2\,g$, there is no pull-in discontinuity and the electrode traverses smoothly over the entire gap.

1.2.3 Deflection

The lumped model for electrostatic actuators has analytical solutions for steady state deflection. By expanding and cross multiplying the terms of Eq. 1.6, it can be written in the following form.

$$z^3 - 2\left(g + \frac{t_d}{\epsilon_r}\right)\,z^2 + \left(g + \frac{t_d}{\epsilon_r}\right)^2 z - \left(\frac{\epsilon_0\,A\,V^2}{2\,k}\right) = 0 \tag{1.10}$$

The above equation is a cubic algebraic equation in z and is solved through the standard solution procedures [25, 26]. The following variables are defined in order to represent the

final solutions in a convenient form.

$$\hat{g} = g + \frac{td}{\epsilon_r}; \qquad l = \frac{\epsilon_0 A}{2k}; \qquad n = \frac{2\hat{g}}{3};$$
$$u = \left(\frac{\hat{g}}{3}\right)^2; \qquad w = \left(\frac{\hat{g}^3}{27} - l V^2\right);$$
$$P = \left(w + \sqrt{w^2 - u^3}\right)^{1/3}$$
$$Q = \left(w - \sqrt{w^2 - u^3}\right)^{1/3}$$

The three solutions of Eq. 1.10 in terms of the above defined variables are as follows.

$$z_1 = -(P+Q) + \frac{2\hat{g}}{3} \tag{1.11}$$
$$z_2 = \frac{1}{2}(P+Q) + i\frac{\sqrt{3}}{2}(P-Q) + \frac{2\hat{g}}{3} \tag{1.12}$$
$$z_3 = \frac{1}{2}(P+Q) - i\frac{\sqrt{3}}{2}(P-Q) + \frac{2\hat{g}}{3} \tag{1.13}$$

The behaviour of these solutions is illustrated by considering examples with $k = 4N/m$, $A = 250 \times 50\,\mu m^2$, $g = 1.5\,\mu m$, $\epsilon_r = 4.5$ and for varying dielectric layer thickness. The values of P and Q are found to be complex conjugates and hence, all the three solutions are real. Fig. 1.2 shows the solutions when there is no dielectric layer. z_1, z_2 and z_3 are shown by the solid, dashed and dotted lines respectively. z_1 is a stable equilibrium solution and z_2 is an unstable equilibrium solution. The stability of these solutions can be determined from the approach discussed in chapter 5. z_3 is an infeasible solution since the deflection value cannot exceed g. Note that at $z = \frac{g}{3}$, pull-in occurs and stable equilibrium solution does not exist beyond this deflection. Fig. 1.3 shows the possible solutions at different values of dielectric layer thickness. The parameter h in the figure is proportional to the dielectric thickness and is defined as,

$$h = \frac{t_d}{g\,\epsilon_r}. \tag{1.14}$$

Note that with the increase in dielectric layer thickness, the stable operating distance

increases and for $h \geq 2$, the actuator traverses smoothly over the entire distance without any discontinuity.

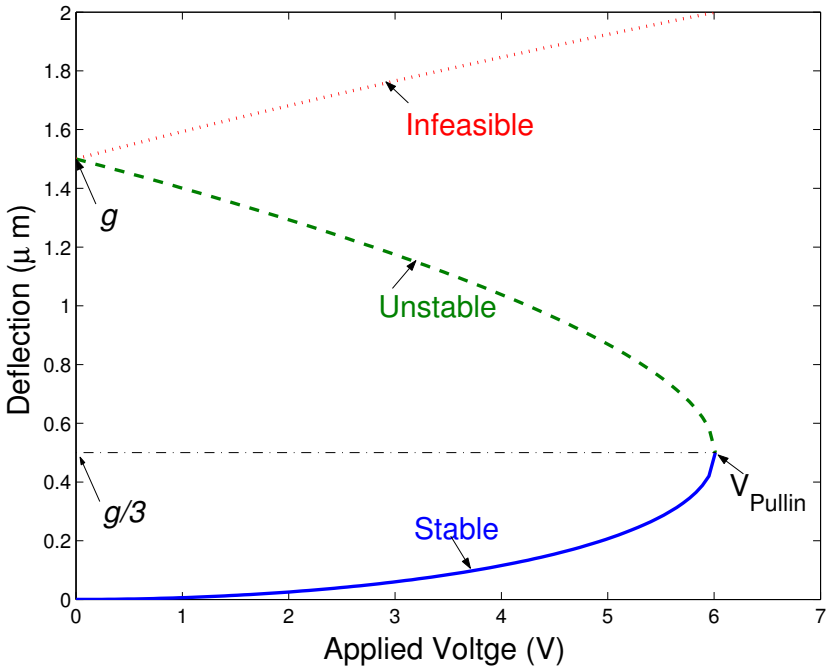

Figure 1.2: Solutions of MEMS electrostatic actuator without dielectric layer

1.2.4 Applications

Two of the important applications of MEMS parallel plate actuators are as variable capacitors (varactors) and RF switches.

MEMS Varactor

Varactor application requires a continuous and reversible variation in capacitance with the applied voltage. Due to the discontinuous transition at the pull-in voltage, the capacitance variations till pull-in can only be utilized for varactor applications in the pull-in regime. Tunability is defined as

$$\text{Tunability} = \left(\frac{C_{max} - C_{min}}{C_{min}} \right) \times 100 \tag{1.15}$$

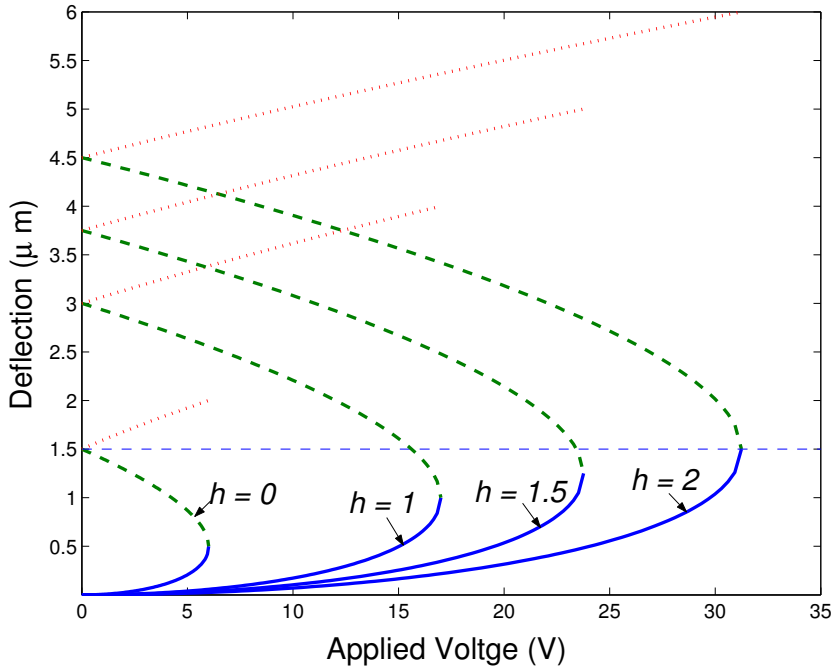

Figure 1.3: Solutions of MEMS electrostatic actuator for different dielectric layer thickness values

where C_{max} and C_{min} are the maximum and minimum capacitances respectively. Capacitance is minimum when no voltage is applied and is given by

$$C_{min} = \frac{\epsilon_0 A}{g + \frac{t_d}{\epsilon_r}}. \tag{1.16}$$

For $h \leq 2$, the upper electrode traverses a maximum distance of $\frac{1}{3}\left(g + \frac{t_d}{\epsilon_r}\right)$ before the pull-in and the corresponding maximum capacitance is

$$C_{max} = \frac{3\,\epsilon_0 A}{2\left(g + \frac{t_d}{\epsilon_r}\right)}. \tag{1.17}$$

Substituting Eq. 1.16 & 1.17 in Eq. 1.15, the tunability is found to be 50%. Note that C_{max} value for all values of $h > 2$ is constant since the maximum deflection cannot exceed g and given by

$$C_{max} = \frac{\epsilon_0\,\epsilon_r\,A}{t_d}. \tag{1.18}$$

On the other hand, C_{min} always decreases with the increase in h.

Hence, for $h \leq 2$, tunability for varactor applications (in the pull-in regime) is constant and is 50% whereas for $h > 2$, tunability decreases with the increase in dielectric thickness. Fig 1.4 shows the capacitance-voltage (C-V) characteristics for different values of dielectric layer thickness. The capacitance values are normalized with respect to C_{min}.

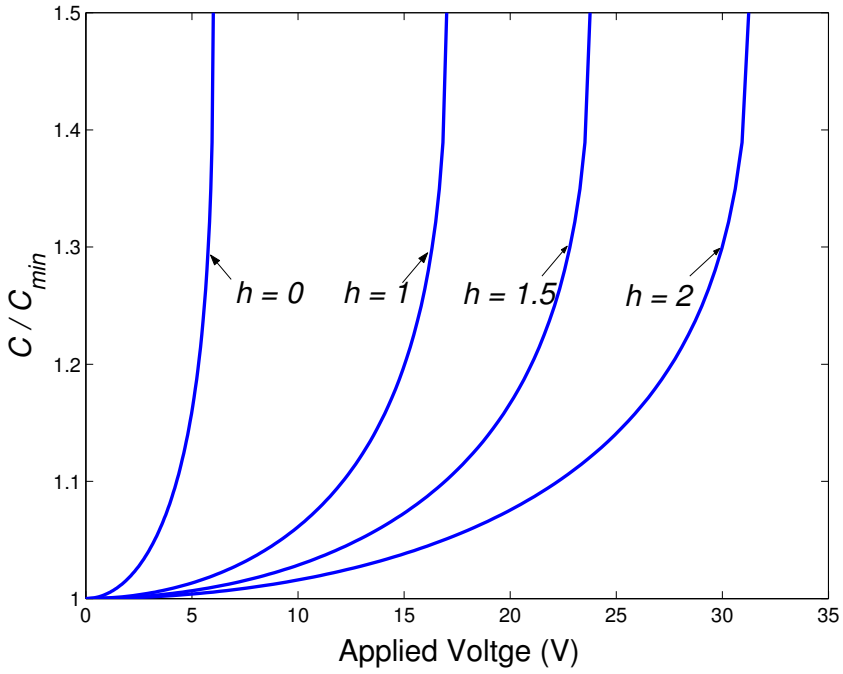

Figure 1.4: C-V characteristics of MEMS electrostatic actuator for different dielectric layer thickness values

MEMS Switch

MEMS switches are the devices that use mechanical movement to achieve a short circuit or an open circuit in the RF transmission line. RF MEMS switches are the specific micromechanical switches that are designed to operate RF to millimeter-wave frequencies (0.1 to 100 GHz) [13, 27]. MEMS switches have several advantages over p-i-n or FET switches like low power consumption, large down-to-up-state capacitance ratios, low inter-modulation products and very low costs. The up-state capacitance is same as C_{min} and is

$$C_u = \frac{\epsilon_0 A}{g + \frac{t_d}{\epsilon_r}}. \tag{1.19}$$

When the applied voltage exceeds pull-in voltage, the upper plate comes in contact with the dielectric layer and the corresponding down-state capacitance is given by

$$C_d = \frac{\epsilon_0 \, \epsilon_r \, A}{t_d}. \tag{1.20}$$

The down-state/up-state capacitance ratio is

$$\frac{C_d}{C_u} = \left(1 + \frac{\epsilon_r \, g}{t_d}\right). \tag{1.21}$$

The capacitance ratio increases with the decrease in dielectric layer thickness. However, it is impractical to deposit a dielectric layer which is thinner than 100 A° [13] due to pin-hole problems in dielectric layers. Also, dielectric layer must be able to withstand the actuation voltage without dielectric breakdown.

1.2.5 Limitations of Lumped Model

In the lumped spring-mass-damper model discussed so far, the upper electrode completely comes in contact with the dielectric layer at the pull-in voltage it self. There is no further change in the deflection of this model beyond the pull-in voltage. Hence this model is not useful in understanding the behaviour of the actuators beyond the pull-in. Further, the magnitudes of tunability, pull-in voltage, capacitance ratio and other numerical limits that are computed above using the lumped model deviate considerably with the actual values. Hence, all further analysis in this thesis is carried out using a 1-D beam model along with a dielectric layer.

1.3 Thesis Organization

The thesis is organized as follows. In chapter 2, we present the details of mathematical modeling and numerical simulations using modal expansion method and finite difference scheme. In chapter 3, we study the effects of an intermediate dielectric layer on the transitions and bi-stable states of the actuator. In chapter 4, dynamic stability analysis

of equilibrium solutions is performed for two of the configurations. In chapter 5, a case study example is considered and the results are analyzed. Finally, chapter 6 summarizes the conclusions of the analysis and future scope of the work.

Chapter 2

Mathematical Modeling and Simulations

2.1 Introduction

In this thesis, we study the behaviour of cantilever beam MEMS electrostatic actuators beyond the pull-in. Simple lumped-element models fail to capture the behaviour beyond the pull-in. Hence, the analysis is performed using a 1-D beam model. This chapter presents the details of the possible configurations along with the boundary conditions, governing equation, normalization and simulation techniques that uses modal expansion method and finite difference method. A scaling law observed in the flat configuration is also presented.

2.2 Possible Configurations

The cantilever beam electrostatic actuator is illustrated in Fig. 2.1. It has three possible configurations in the entire operational range. These configurations differ in the boundary conditions at the free end of the cantilever beam and are as follows.

1. Floating Configuration: The cantilever beam has no contact with the dielectric layer and is illustrated in Fig. 2.2(a). The bending moment and shear force at the free

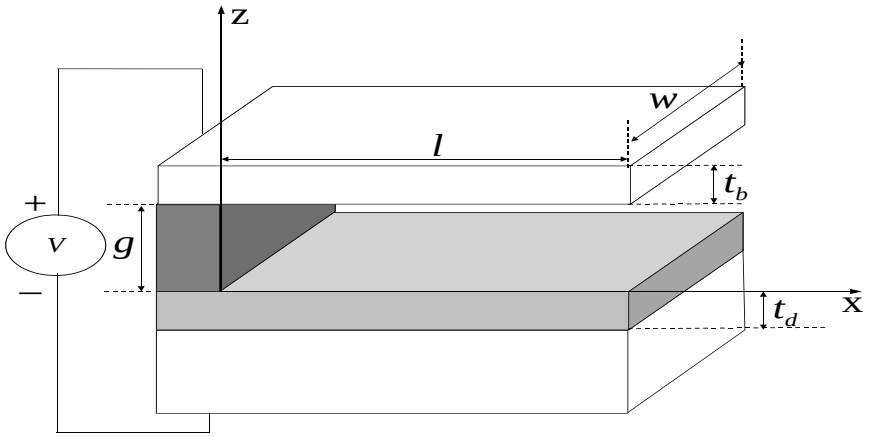

Figure 2.1: Schematic view of the cantilever beam electrostatic actuator.

end are zero.

2. Pinned Configuration: The free end of the cantilever beam touches the dielectric layer but is free to pivot about the contact point and is illustrated in Fig. 2.2(b). The deflection (measured from the dielectric layer) and the bending moment are zero at the touching end.

3. Flat Configuration: A non-zero length of the beam is in contact with the dielectric layer, as illustrated in Fig. 2.2(c). The contact length of the cantilever beam varies with the applied voltage. Deflection measured from the dielectric layer, slope and moment are zero at the point separating the contact and the non-contact regions of the cantilever. The point is denoted by $x = a$ in Fig. 2.2(c). Note that, unlike the previous two configurations, The shear force is the only unknown boundary condition at this point. Here the extent of the domain (the non-contacting region) is not known in advance; the previous two configurations represent boundary value problems, while the flat configuration represents a free boundary problem. We will not concern ourselves unduly with this distinction, as will be seen below.

The boundary conditions discussed so far are summarized in Table 2.1. The parameter l in the table denotes the length of the beam. At the clamped end of the cantilever beam, the boundary conditions are the same for all the configurations: the slope is zero and

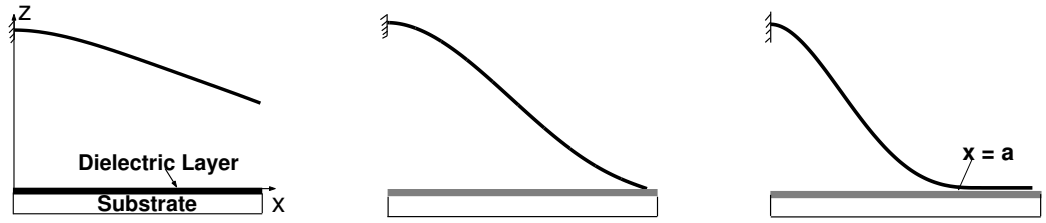

(a) Floating configuration. (b) Pinned configuration. (c) Flat configuration.

Figure 2.2: Possible configurations of the cantilever beam actuator. (The scale in the vertical direction is exaggerated.)

Table 2.1: Boundary conditions at the free end of the cantilever beam for the three configurations.

Type of configuration	Boundary conditions
Floating	$z''(l) = 0;\ z'''(l) = 0$
Pinned	$z(l) = 0;\ z''(l) = 0$
Flat	$z(a) = 0;\ z'(a) = 0;\ z''(a) = 0$

the deflection (measured from the dielectric layer) is equal to the zero bias height of the cantilever beam (g).

Note that pinned and flat configurations are also called arc-type and S-type respectively in the literature [28, 29].

The non-contact portion of the beam for all the three configurations is governed by the same equation.

2.3 Governing Equation

The 1-D equation governing the mechanical deformation of an Euler-Bernoulli beam is

$$E\,I\,\frac{\partial^4 z}{\partial x^4} + \rho\,\frac{\partial^2 z}{\partial t^2} = F_e \tag{2.1}$$

$$\text{where} \quad F_e \;=\; -\frac{\epsilon_0\, w\, V^2}{2\left(z + \dfrac{t_d}{\epsilon_r}\right)^2} \tag{2.2}$$

Table 2.2: Description of the parameters in the governing equation.

Parameter	Description
l	Beam length
w	Beam width
t_b	Beam thickness
t_d	Dielectric layer thickness
ρ	Mass per unit length of the beam
g	Zero bias height of the cantilever beam
A	Beam cross-sectional area ($= w\,t_b$)
I	Moment of inertia of the beam cross-section $\left(= \frac{w\,t_b^3}{12}\right)$
E	Young's modulus of the beam material
ϵ_0	Permittivity of free space
ϵ_r	Relative permittivity of the dielectric or dielectric constant
V	Applied voltage

F_e is the electrical force per unit length. The derivation for F_e is along the lines of derivation in section 1.2.1 except that there is a change in the sign convention of coordinate axes. The variables x and z in the above equations denote the position along the length and the lateral deflection of the beam respectively; and t is time. Effects like step-ups, stress-stiffening and softened contact surfaces are not included in this model. The parameters in the governing equation are described in Table 2.2.

The common practice [7] of using a fringing field correction such as $0.65\,\frac{(z+t_d/\epsilon_r)}{w}$ is not adopted here. In the post-pull-in regime, the cantilever beam has portions very close to the dielectric, where the fringing field is small. Further, neglecting the fringing field makes the analysis simpler and provides useful insights. Finally, calculations including the fringing field, though slightly complex, could if necessary be carried out using the approach adopted in this thesis.

2.4 Normalized Equation

The length quantities x and z (refer to Fig. 2.1) are normalized with respect to the length and zero bias height of the beam. Time t is normalized with respect to a constant T, defined in such a way that the parameter ρ in Eq. 2.1 becomes unity. All the further

analysis is carried out on the normalized equation and the results thus obtained are finally scaled to the actual parameters. The normalized quantities are as follows.

$$\hat{x} = \frac{x}{l} \tag{2.3}$$

$$\hat{z} = \frac{z}{g} \tag{2.4}$$

$$\hat{t} = \frac{t}{T} \tag{2.5}$$

$$\text{where } T = \sqrt{\frac{\rho\, l^4}{E\, I}} \tag{2.6}$$

Two other non-dimensional quantities are defined as follows.

$$\hat{V} = \sqrt{\frac{\epsilon_0 w\, l^4}{2\, E\, I\, g^3}}\, V, \tag{2.7}$$

$$h = \frac{t_d}{g\, \epsilon_r}. \tag{2.8}$$

The governing equation becomes

$$\frac{\partial^4 \hat{z}}{\partial \hat{x}^4} + \frac{\partial^2 \hat{z}}{\partial \hat{t}^2} = -\frac{\hat{V}^2}{(\hat{z}+h)^2} \tag{2.9}$$

For static analysis, there is no time dependence and the equation reduces to

$$\frac{d^4 \hat{z}}{d\hat{x}^4} = -\frac{\hat{V}^2}{(\hat{z}+h)^2} \tag{2.10}$$

The hats in the normalized equation are dropped for convenience in the following analysis.

The following sections present the details simulation techniques.

2.5 Modal Expansion Method

2.5.1 Modal Expansion Method in General

The coupled electro-mechanical equation of the electrostatically actuated beams (Eq. 2.10) can be solved using modal expansion method. The deflection of the beam is expressed as a superposition of its modes. The modes are constructed in such a way that the mechanical force per unit length on any mode is proportional to the mode deflection. So, if the force per unit length on a mode is known, the corresponding deflection can be calculated by multiplying it with the suitable proportionality constant and vice versa. Mechanical force per unit length (F_{mech}) is the fourth order derivative of beam deflection z. The fourth order derivatives of sin, cos, sinh and cosh functions are proportional to the respective functions themselves. So, each mode is constructed as a combination of these functions. Let

$$\begin{aligned} \psi_j(x) &= j^{th} \text{ mode of the beam.} \\ z(x) &= \text{Beam deflection.} \\ z_0(x) &= \text{Initial position of the beam.} \\ w(x) &= \text{Beam deflection from the initial position.} \end{aligned}$$

$z(x)$ can be expressed as

$$z(x) = z_0(x) + w(x). \tag{2.11}$$

$\psi_j(x)$ is expressed as

$$\psi_j(x) = B_{1j}\,\sin(\lambda_j\,x) + B_{2j}\,\cos(\lambda_j\,x) + B_{3j}\,\sinh(\lambda_j\,x) + B_{4j}\,\cosh(\lambda_j\,x). \tag{2.12}$$

The values of B_{1j}, B_{2j}, B_{3j},B_{4j} and λ_j are evaluated from the boundary conditions. $w(x)$ is expressed as

$$w(x) = \sum_{j=1}^{N} a_j\,\psi_j(x). \tag{2.13}$$

$$\Rightarrow z(x) = z_0(x) + \sum_{j=1}^{N} a_j\,\psi_j(x) \tag{2.14}$$

where a_j is the participation factor associated with the j^{th} mode and is called *modal amplitude* of j^{th} mode.

When the applied voltage is zero,

$$z(x) = z_0(x).$$

Then the mechanical force per unit length should also be zero.

$$\Rightarrow F_{mech} = \frac{d^4 z}{dx^4} = \frac{d^4 z_0}{dx^4} = 0$$

$$\Rightarrow \frac{d^4 z_0}{dx^4} = 0 \tag{2.15}$$

So, mechanical force per unit length can be expressed as

$$F_{mech} = \frac{d^4 z}{dx^4} = \frac{d^4 w}{dx^4} = \sum_{j=1}^{N} \lambda_j^4 \, a_j \, \psi_j(x). \tag{2.16}$$

The boundary conditions at the clamped end are same for all the configurations and are

$$z(0) = 1 \Rightarrow \psi_j(0) = 0$$

$$z'(0) = 0 \Rightarrow \psi_j'(0) = 0.$$

From these boundary conditions and by taking $B_{4j} = 1$, $B_{3j} = B_j$, Eq. 2.12 reduces to the following form.

$$\psi_j(x) = \cosh(\lambda_j \, x) - \cos(\lambda_j \, x) - B_j \left(\sinh(\lambda_j \, x) - \sin(\lambda_j \, x)\right) \tag{2.17}$$

B_j and λ_j are computed from the boundary conditions at the free end of the cantilever beam. The derivatives of ψ_j w.r.t. x are

$$\psi_j'(x) = \lambda_j \left(\sinh\left(\lambda_j\, x\right) + \sin\left(\lambda_j\, x\right) - B_j \left(\cosh\left(\lambda_j\, x\right) - \cos\left(\lambda_j\, x\right)\right)\right) \tag{2.18}$$

$$\psi_j''(x) = \lambda_j^2 \left(\cosh\left(\lambda_j\, x\right) + \cos\left(\lambda_j\, x\right) - B_j \left(\sinh\left(\lambda_j\, x\right) + \sin\left(\lambda_j\, x\right)\right)\right) \tag{2.19}$$

$$\psi_j'''(x) = \lambda_j^3 \left(\sinh\left(\lambda_j\, x\right) - \sin\left(\lambda_j\, x\right) - B_j \left(\cosh\left(\lambda_j\, x\right) + \cos\left(\lambda_j\, x\right)\right)\right) \tag{2.20}$$

$$\psi_j''''(x) = \lambda_j^4 \left(\cosh\left(\lambda_j\, x\right) - \cos\left(\lambda_j\, x\right) - B_j \left(\sinh\left(\lambda_j\, x\right) - \sin\left(\lambda_j\, x\right)\right)\right) = \lambda_j^4 \psi_j(x). \tag{2.21}$$

The modes possess the following *orthogonality relation*:

$$\int_0^1 \psi_i(x)\, \psi_j(x)\, dx = \begin{cases} 1 & \text{if } i = j \\ 0 & \text{Otherwise} \end{cases} \tag{2.22}$$

Computation of Modal Amplitudes

The modal amplitudes are computed using the orthogonality relation in Eq. 2.22. The procedure is as follows:

Multiplying Eq. 2.16, with $\psi_i(x)$ on both sides and integrating from 0 to 1 w.r.t x,

$$\int_0^1 F_{mech}\, \psi_i(x)\, dx = \int_0^1 \sum_{j=1}^{N} a_j\, \psi_j(x)\, \psi_i(x)\, dx.$$

Interchanging summation and integration on the right hand side of the above equation,

$$\begin{aligned} \int_0^1 F_{mech}\, \psi_i(x)\, dx &= \sum_{j=1}^{N} \int_0^1 a_j \psi_j(x)\, \psi_i(x)\, dx \\ \Rightarrow \int_0^1 F_{mech}\, \psi_i(x)\, dx &= \sum_{\substack{j=1 \\ j\neq i}}^{N} a_j \int_0^1 \psi_j(x)\, \psi_i(x)\, dx + a_i \int_0^1 \psi_i^2(x)\, dx. \end{aligned}$$

From the orthogonality relation in Eq. 2.22, above equation reduces to to the following form.

$$a_i = \int_0^1 F_{mech}\, \psi_i(x)\, dx \tag{2.23}$$

In this equation, i is varied from 1 to N and the corresponding modal amplitudes are computed.

The boundary conditions of the configurations are discussed in section 2.2 and are summarized in Table 2.1. The necessary equations for solving the floating and pinned configurations are derived in the following subsections.

2.5.2 Floating Configuration

Each mode of the floating configuration shown in Fig. 2.2(a) has to satisfy the following boundary conditions at $x = 1$.

$$\psi_j''(1) = 0 \tag{2.24}$$

$$\psi_j'''(1) = 0 \tag{2.25}$$

From Eq. 2.19 and 2.24,

$$\cosh(\lambda_j) + \cos(\lambda_j) - B_j\left(\sinh(\lambda_j) + \sin(\lambda_j)\right) = 0. \tag{2.26}$$

From Eq. 2.20 and 2.25,

$$\sinh(\lambda_j) - \sin(\lambda_j) - B_j\left(\cosh(\lambda_j) + \cos(\lambda_j)\right) = 0. \tag{2.27}$$

B_j from Eq. 2.27 is

$$B_j = \frac{\sinh(\lambda_j) - \sin(\lambda_j)}{\cosh(\lambda_j) + \cos(\lambda_j)}. \tag{2.28}$$

For high values of λ_j, $\sinh(\lambda_j)$ and $\cosh(\lambda_j)$ are approximately equal and are very large compared to $\sin(\lambda_j)$ and $\cos(\lambda_j)$. Hence, B_j approches unity for large values of λ_j.

Table 2.3: Roots and coefficient values of various modes of the floating configuration.

Modes of Vibration (j)	λ_j	B_j
1	1.8751	0.73409
2	4.6941	1.01847
3	7.8548	0.99922
4	10.9955	$1 + 3.35 \times 10^{-5}$
5	14.1372	1
6	17.2788	1

Substituting B_j in Eq. 2.26,

$$\begin{aligned} \cosh(\lambda_j) + \cos(\lambda_j) - \frac{\sinh(\lambda_j) - \sin(\lambda_j)}{\cosh(\lambda_j) + \cos(\lambda_j)} (\sinh(\lambda_j) + \sin(\lambda_j)) &= 0 \\ \Rightarrow \cosh^2(\lambda_j) + \cos^2(\lambda_j) + 2\cosh(\lambda_j)\cos(\lambda_j) - \sinh^2(\lambda_j) + \cos^2(\lambda_j) &= 0 \end{aligned}$$

$$\Rightarrow 1 + \cosh(\lambda_j)\cos(\lambda_j) = 0 \tag{2.29}$$

Eq. 2.29 is the characteristic equation of the floating configuration. The roots of the characteristic equation can be determined using numerical methods like Newton-Raphson method. Table 2.3 summarizes the roots (λ_j) and the coefficient values (B_j) of the first six modes of operation.

Deflection of the beam

The initial position of the floating configuration is

$$\begin{aligned} z_0(x) &= 1 \\ \Rightarrow z(x) &= 1 + \sum_{j=1}^{N} a_j \psi_j(x) \end{aligned} \tag{2.30}$$

2.5.3 Pinned Configuration

Each mode of the pinned configuration shown in Fig. 2.2(b) has to satisfy the following boundary conditions at $x = 1$.

$$\psi_j(1) = 0 \tag{2.31}$$

$$\psi_j''(1) = 0 \tag{2.32}$$

From Eq. 2.17 and 2.31,

$$\cosh(\lambda_j) - \cos(\lambda_j) - B_j(\sinh(\lambda_j) - \sin(\lambda_j)) = 0. \tag{2.33}$$

From Eq. 2.19 and 2.32,

$$\cosh(\lambda_j) + \cos(\lambda_j) - B_j(\sinh(\lambda_j) + \sin(\lambda_j)) = 0. \tag{2.34}$$

Adding Eq. 2.33 & 2.34 and solving for B_j,

$$B_j = \coth(\lambda_j). \tag{2.35}$$

For large values of λ_j, $\cosh(\lambda_j)$ and $\sinh(\lambda_j)$ are approximately equal and hence, B_j approches unity.
Substituting B_j in Eq. 2.33,

$$\cosh(\lambda_j)\sin(\lambda_j) - \sinh(\lambda_j)\cos(\lambda_j) = 0.$$

Dividing the above equation by $\sinh(\lambda_j)\sin(\lambda_j)$,

$$\coth(\lambda_j) - \cot(\lambda_j) = 0. \tag{2.36}$$

Eq. 2.36 is the characteristic equation of the pinned configuration. Table 2.4 summarizes the roots (λ_j) and the coefficient values (B_j) of the first six modes of operation.

Table 2.4: Roots and coefficient values of various modes of the pinned configuration.

Modes of Vibration (j)	λ_j	B_j
1	3.9266	$1 + 7.8 \times 10^{-4}$
2	7.0686	1
3	10.2102	1
4	13.3518	1
5	16.4934	1
6	19.6350	1

Deflection of the beam

Let the initial position of the beam in pinned configuration be expressed as a polynomial in x as follows.

$$z_0(x) = a_0 + a_1 x + a_2 x^2 + a_3 x^3 + a_4 x^4 + \cdots + a_n x^n \tag{2.37}$$

When no voltage is applied, from Eq. 2.15 and 2.37,

$$\begin{aligned} a_4 = a_5 = \cdots = a_n = 0 \\ \Rightarrow z_0(x) = a_0 + a_1 x + a_2 x^2 + a_3 x^3. \end{aligned} \tag{2.38}$$

The boundary conditions at the clamped end are,

$$\begin{aligned} z_0(0) = 1 \Rightarrow a_o = 1 \\ z_0'(0) = 0 \Rightarrow a_1 = 0 \\ \Rightarrow z_0(x) = 1 + a_2 x^2 + a_3 x^3. \end{aligned} \tag{2.39}$$

The boundary conditions at the pinned end are,

$$\begin{aligned} z_0(1) = 0 \Rightarrow 1 + a_2 + a_3 = 0 \\ z_0''(1) = 0 \Rightarrow a_2 + 3a_3 = 0 \end{aligned}$$

Table 2.5: Characteristic equations, coefficient values and Initial position of the beam for various configurations.

Type of configuration	Characteristic Equation	Coefficient value	$z_0(x)$
Floating	$1+\cosh(\lambda_j)\cos(\lambda_j)=0$	$\frac{\sinh(\lambda_j)-\sin(\lambda_j)}{\cosh(\lambda_j)+\cos(\lambda_j)}$	1
Pinned	$\coth(\lambda_j)-\cot(\lambda_j)=0$	$\coth(\lambda_j)$	$1-\frac{3}{2}x^2+\frac{1}{2}x$

Solving the above equations, we get

$$z_0(x) = 1 - \frac{3}{2}x^2 + \frac{1}{2}x^3.$$
$$\Rightarrow z(x) = \left(1 - \frac{3}{2}x^2 + \frac{1}{2}x^3\right) + \sum_{j=1}^{N} a_j \psi_j(x) \tag{2.40}$$

Table 2.5 summarizes the characteristic equations, B_j values and initial positions of the beam for the floating and pinned configurations.

2.5.4 Procedure to Solve the Coupled Equation

The iterative procedure to solve the coupled electro-mechanical equation using modal expansion method is described here.

Input: The dimensions and material properties of the beam, dielectric constant, dielectric layer thickness, zero bias height and the applied voltage are given as inputs to the method.

Initialization: The deflection of the beam from the initial position i.e., $w(x)$ is initialized to zero. In other words, all the modal amplitudes are initialized to zero.

The non-dimensional quantities in the normalized equation are computed and the following steps are followed.

Step 1: Compute Electrostatic Force

Electrostatic force per unit length is computed from the relation

$$F_e = -\frac{V^2}{(z+h)^2}$$

Step 2: Find the Modal Expansion of the Force

All the modal amplitudes (a_i values) of the force are computed from Eq. 2.23.

Step 3: Check the Convergence of Modal Amplitudes

If the maximum of absolute differences between the a_i values before and after Step 2 is greater than tolerance value, go to Step 4.

If it is less than tolerance value, it implies that the solution is converged and the a_j values computed in Step 2 represent the final modal amplitudes. Jump to step 5.

Step 4: Find out the deflection

The beam shape is computed from the relation

$$z(x) - z_0(x) = \sum_{j=1}^{N} \frac{a_j}{\lambda_j^4} \psi_j(x)$$

and the procedure is repeated from Step 2.

Step 5: Output the Results

The results are scaled to the actual input parameters and are outputted.

The above algorithm is illustrated in the flow chart shown in Fig. 2.5.4

2.5.5 Modified Procedure using Newton's Method

The convergence of modal amplitudes in the iterative procedure described in previous subsection can be improved by employing Newton's method [30].

Let $\vec{a}$ denote the vector of modal amplitudes and $\delta\vec{a}$ denote the difference in $\vec{a}$ from the next iteration.

$$\vec{a} = [\, a_1, a_2, a_3, \ldots, a_N \,]^T \tag{2.41}$$

$$\delta\vec{a} = [\, \delta a_1, \delta a_2, \delta a_3, \ldots, \delta a_N \,]^T \tag{2.42}$$

Let $\vec{a}_{new}$ indicate the vector with the modified modal amplitudes.

$$\vec{a}_{new} = \vec{a} + \delta\vec{a} \tag{2.43}$$

$$\Rightarrow \vec{a}_{new} = [\, a_1 + \delta a_1, a_2 + \delta a_2, a_3 + \delta a_3, \ldots, a_N + \delta a_N \,]^T \tag{2.44}$$

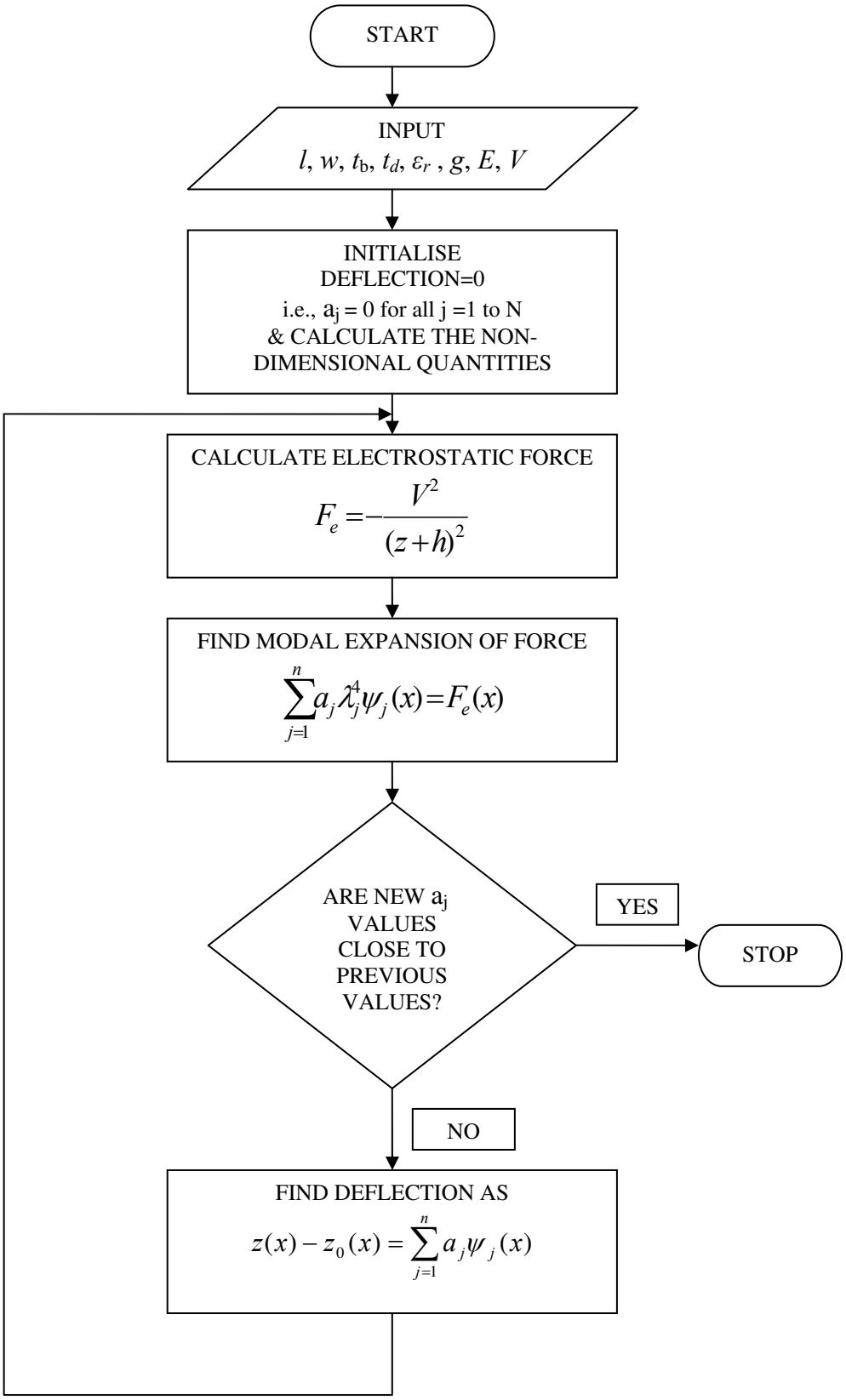

Figure 2.3: Flow chart for Modal Expansion Method.

If $\vec{a}_{new}$ represents the exact modal amplitudes,

$$\sum_{j=1}^{n} (\vec{a}_{new})_j \lambda_j^4 \psi_j(x) = -\frac{V^2}{(z(x)+h)^2} \tag{2.45}$$

where $(\vec{a}_{new})_j$ represents the j^{th} component of $\vec{a}_{new}$.
Multiplying Eq. 2.45 with $\psi_i(x)$ on both sides and integrating from 0 to 1 w.r.t. x,

$$\int_0^1 \sum_{j=1}^{N} (\vec{a}_{new})_j \lambda_j^4 \psi_j(x)\psi_i(x)\, dx = -\int_0^1 \frac{V^2}{(z(x)+h)^2}\psi_i(x)\, dx.$$

The variable i in the above equation can have any value from 0 to N. Interchanging integration and summation on the left hand side of the above equation and using orthogonal relation of modes specified in Eq. 2.22, the above equation reduces to the following form.

$$(\vec{a}_{new})_i \lambda_i^4 = -\int_0^1 \frac{V^2}{(z(x)+h)^2}\psi_i(x)\, dx \tag{2.46}$$

Let

$$F_i(\vec{a}_{new}) = F_i(\vec{a} + \delta\vec{a}) = (\vec{a}_{new})_i \lambda_i^4 + \int_0^1 \frac{V^2}{(z(x)+h)^2}\psi_i(x)\, dx = 0 \tag{2.47}$$

For $i = 1$ to N , we get N such equations. Let

$$\vec{F}(\vec{a}_{new}) = [\, F_1(\vec{a}_{new}), F_2(\vec{a}_{new}), F_3(\vec{a}_{new}), \ldots, F_N(\vec{a}_{new})\,]^T. \tag{2.48}$$

Writing Eq. 2.47 in vector form taking all values of i,

$$\vec{F}(\vec{a} + \delta\vec{a}) = 0 \Rightarrow \vec{F}(\vec{a}) + J\,\delta\vec{a} = 0. \tag{2.49}$$

where J is the Jacobian matrix defined as

$$J_{i,j} = \frac{\partial F_i}{\partial a_j}. \tag{2.50}$$

From Eq. 2.49,

$$\delta\vec{a} = -J^{-1}\,\vec{F}\,(\vec{a}) \tag{2.51}$$

where

$$F_i\,(\vec{a}) = a_i\lambda_i^4 + \int_0^1 \frac{V^2}{(z(x)+h)^2}\psi_i(x)\,dx. \tag{2.52}$$

Let

$$f_i = -\frac{V^2}{(z(x)+h)^2}\,\psi_i(x). \tag{2.53}$$

$$\Rightarrow \frac{\partial f_i}{\partial a_j} = \frac{\partial f_i}{\partial z}\,\frac{\partial z}{\partial a_j} \tag{2.54}$$

Substituting Eq. 2.53 in Eq. 2.52,

$$F_i\,(\vec{a}) = a_i\,\lambda_i^4 - \int_0^1 f_i\,dx. \tag{2.55}$$

From Eq. 2.53,

$$\frac{\partial f_i}{\partial z} = \frac{2V^2}{(z(x)+h)^3}\psi_i(x).$$

From Eq. 2.14,

$$\frac{\partial z}{\partial a_j} = \psi_j(x).$$

$$\Rightarrow \frac{\partial f_i}{\partial a_j} = \frac{2V^2}{(z(x)+h)^3}\psi_i(x)\,\psi_j(x) \tag{2.56}$$

From Eq. 2.55 and 2.56,

$$\frac{\partial F_i}{\partial a_j} = \begin{cases} \lambda_i^4 - \int_0^1 \frac{\partial f_i}{\partial a_j}\,dx & \text{if } i = j \\ -\int_0^1 \frac{\partial f_i}{\partial a_j}\,dx & \text{Otherwise.} \end{cases} \tag{2.57}$$

From Eq. 2.50, 2.56 and 2.57,

$$J_{i,j} = \begin{cases} \lambda_i^4 - \int_0^1 \frac{2V^2}{(z(x)+h)^3}\psi_i^2(x)\,dx & \text{if } i = j \\ -\int_0^1 \frac{2V^2}{(z(x)+h)^3}\psi_i(x)\,\psi_j(x)\,dx & \text{Otherwise.} \end{cases} \tag{2.58}$$

From the above equation, it is evident that

$$\frac{\partial F_i\left(\vec{a}\right)}{\partial a_j} = \frac{\partial F_j\left(\vec{a}\right)}{\partial a_i} \Rightarrow J_{i,j} = J_{j,i}. \tag{2.59}$$

Hence, Jacobian in this case is a *symmetric matrix*.

Algorithm

The input and the initialization part are similar to the general method discussed in the previous subsection. The steps are as follows:

Step 1: Compute $F_i\left(\vec{a}\right)$ from Eq. 2.52, for all values of i from 1 to N

Step 2: Compute Jacobian matrix J from Eq. 2.58, and $\delta\vec{a}$ from Eq. 2.51.

Step 3: If $\max(\text{abs}(\delta\vec{a})) <$ tolerance value, the solution is converged and jump to Step 5. else, go to Step 4

Step 4: $\vec{a}_{new}$ is computed from Eq. 2.43. $\vec{a}$ is replaced with $\vec{a}_{new}$ and the the procedure repeated from Step 1.

Step 5: The results are scaled to the actual input parameters and are outputted

The above procedure is illustrated in detail in the flow chart shown in Fig. 2.5.5

Finite difference scheme is developed in the following section to solve all the three configurations.

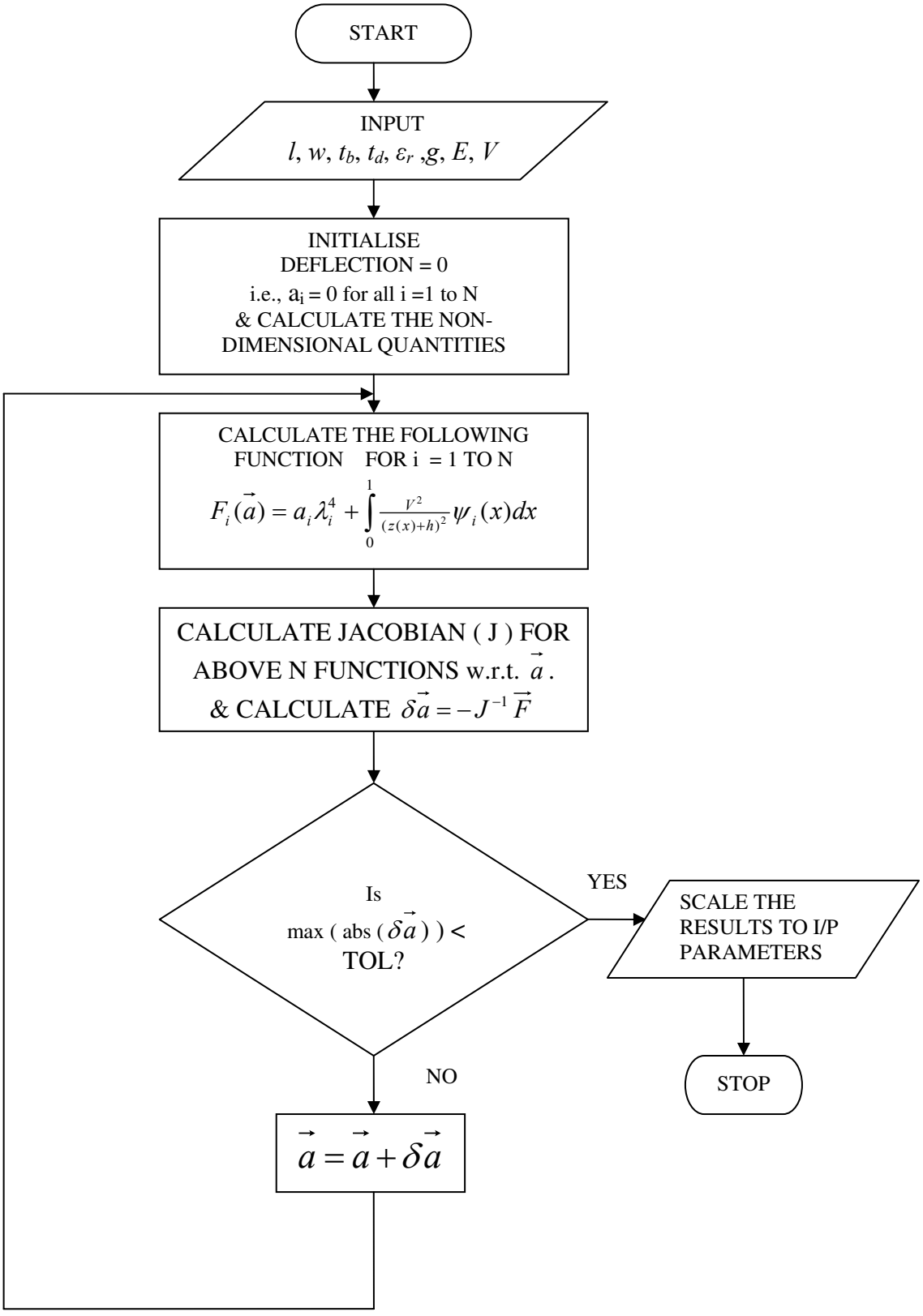

Figure 2.4: Flow chart for Modal Expansion Method that employs Newton's Method.

2.6 Finite Difference Approximation

2.6.1 Method

In finite difference (F.D.) scheme, the derivatives are replaced by finite difference approximations and the resulting system of algebraic equations is solved. Where the boundary conditions involve derivatives, we introduce suitable fictitious points beyond the physical boundaries.

Specifically, a five point central difference scheme is implemented because a fourth order derivative is involved. Two fictitious points are introduced on each side of the non-contact length of the cantilever beam.

The governing Eq. 2.10 to be solved can be wriiten as,

$$\frac{d^4z}{dx^4} + \frac{V^2}{(z+h)^2} = 0. \tag{2.60}$$

The non-contact length of the cantilever beam is divided into a uniform grid of N points along the x-axis with a step size of Δx. These points are denoted by $x_1,\ x_2,\ \cdots\ x_{N-1},\ x_N$. Let z_i denote the beam deflection at $x = x_i$, $i = 1, 2, \cdots, N$. Let the fictitious points be denoted by z_0, z_{-1} on the left side and z_{N+1}, z_{N+2} on the right side of the non-contact length with the same step size, Δx. Hence, totally $N + 4$ points are considered along the x-axis.

Finite diiference approximations are derived as follows. From Taylor's series expansion, z values at x_{i+1}, x_{i-1}, x_{i+2}, x_{i-2} can be written as,

$$z_{i+1} = z_i + (\Delta x)\ z_i' + \frac{(\Delta x)^2}{2} z_i'' + \frac{(\Delta x)^3}{6} z_i''' + \frac{(\Delta x)^4}{24} z_i'''' \tag{2.61}$$

$$z_{i-1} = z_i - (\Delta x)\ z_i' + \frac{(\Delta x)^2}{2} z_i'' - \frac{(\Delta x)^3}{6} z_i''' + \frac{(\Delta x)^4}{24} z_i'''' \tag{2.62}$$

$$z_{i+2} = z_i + 2\ (\Delta x)\ z_i' + \frac{4\ (\Delta x)^2}{2} z_i'' + \frac{8\ (\Delta x)^3}{6} z_i''' + \frac{16\ (\Delta x)^4}{24} z_i'''' \tag{2.63}$$

$$z_{i-2} = z_i - 2\ (\Delta x)\ z_i' + \frac{4\ (\Delta x)^2}{2} z_i'' - \frac{8\ (\Delta x)^3}{6} z_i''' + \frac{16\ (\Delta x)^4}{24} z_i''''. \tag{2.64}$$

The finite difference approximations of the derivatives are computed by solving the above

equations and are as follows.

$$z_i' = \frac{z_{i-2} - 8\,z_{i-1} + 8\,z_{i+1} - z_{i+2}}{12\ (\Delta x)} \tag{2.65}$$

$$z_i'' = \frac{-z_{i-2} + 16\,z_{i-1} - 30\,z_i + 16\,z_{i+1} - z_{i+2}}{12\ (\Delta x)^2} \tag{2.66}$$

$$z_i''' = \frac{-z_{i-2} + 2\,z_{i-1} - 2\,z_{i+1} + z_{i+2}}{2\ (\Delta x)^3} \tag{2.67}$$

$$z_i'''' = \frac{z_{i-2} - 4\,z_{i-1} + 6\,z_i - 4\,z_{i+1} + z_{i+2}}{(\Delta x)^4} \tag{2.68}$$

for $i = 1, 2, \cdots N$.

The governing Eq. 2.60 in terms of finite differences is

$$z_{i-2} - 4\,z_{i-1} + 6\,z_i - 4\,z_{i+1} + z_{i+2} + \frac{(\Delta x)^4\ V^2}{(z_i + h)^2} = 0. \tag{2.69}$$

The solution procedure to solve the system of nonlinear algebraic equations is described below. Newton's method [30] is used to improve the convergence of the solution scheme.

$$\text{Let } z = [\, z_{-1},\, z_0,\, z_1,\, \ldots\, z_N,\, z_{N+1},\, z_{N+2}\,]^T \tag{2.70}$$

$$f_i(z) = z_{i-2} - 4\,z_{i-1} + 6\,z_i - 4\,z_{i+1} + z_{i+2} + \frac{(\Delta x)^4\,V^2}{(z_i + h)^2}, \quad \text{for } i = 1\text{to } N. \tag{2.71}$$

Let $F(z)$ be defined as

$$F(z) = [\, f_1(z),\, f_2(z),\, \ldots\, f_N(z),\, f_{N+1}(z),\, f_{N+2}(z),\, f_{N+3}(z),\, f_{N+4}(z)\,]^T. \tag{2.72}$$

f_1 to f_N are computed from Eq. 2.71 and f_{N+1} to f_{N+4} are computed from the boundary conditions of the corresponding configurations as described later.

$$\text{Let} \qquad \delta z = [\, \delta z_{-1},\, \delta z_0,\, \delta z_1,\, \ldots\, \delta z_{N+2}\,]^T \tag{2.73}$$

be the correction vector such that $F(z + \delta z) = 0$.

$$\Rightarrow F(z) + J\,\delta z = 0 \tag{2.74}$$

where J is the Jacobian matrix with,

$$J_{i,\,j} = \frac{\partial f_i}{\partial z_j}, \qquad \text{for } i = 1 \text{ to } N+4,\ j = -1 \text{ to } N+2. \tag{2.75}$$

From Eq. 2.74,

$$\delta z = -J^{-1}\, F(z). \tag{2.76}$$

The non-zero elements of Jacobian matrix for $i = 1$ to N can be computed from the derivatives Eq. 2.71 and are as follows:

$$\begin{aligned} J_{i,\,i-2} &= J_{i,\,i+2} = 1\,; \\ J_{i,\,i-1} &= J_{i,\,i+1} = -4\,; \\ J_{i,\,i} &= 6 - \frac{2\,(\Delta x)^4\, V^2}{(z_i + h)^3}. \end{aligned} \tag{2.77}$$

The elements of J and F for $i = N{+}1$ to $N{+}4$ are computed from boundary conditions and hence, they are configuration specific. These details along with the solution procedure are presented in the following subsections.

2.6.2 Floating Configuration

At the clamped end of the cantilever beam, deflection is 1 and slope is 0. Replacing the derivatives in the boundary conditions by finite differences and considering them as f_{N+1} and f_{N+2},

$$f_{N+1} = z_1 - 1 \tag{2.78}$$

$$f_{N+2} = z_{-1} - 8\,z_0 + 8\,z_2 - z_3 \tag{2.79}$$

At the free end, bending moment (z'') and shear force (z''') are zero. Replacing these derivatives by finite differences, we get the following equations.

$$f_{N+3} = -z_{N-2} + 16\, z_{N-1} - 30\, z_N + 16 z_{N+1} - z_{N+2} \tag{2.80}$$

$$f_{N+4} = -z_{N-2} + 2\, z_{N-1} - 2\, z_{N+1} + z_{N+2} \tag{2.81}$$

The non-zero values of Jacobian matrix for these boundary conditions are

$$J_{N+1,\,1} = 1\,; \tag{2.82}$$

$$J_{N+2,\,-1} = 1\,;\; J_{N+2,\,0} = -8\,;\; J_{N+2,\,2} = 8\,;\; J_{N+2,\,3} = -1\,; \tag{2.83}$$

$$J_{N+3,\,N-2} = J_{N+3,N+2} = -1\,;\; J_{N+3,\,N-1} = J_{N+3,N+1} = 16\,;\; J_{N+3,\,N)} = -30\,; \tag{2.84}$$

$$J_{N+4,\,N-2} = -1\,;\; J_{N+4,\,N-1} = 2\,;\; J_{N+4,\,N+1} = -2\,;\; J_{N+4,\,N+2} = 1\,; \tag{2.85}$$

In this configuration, the non-contact length is known and is equal to 1 for the normalized case. Hence, z value at $N+4$ points are the only unknowns. The system of $N+4$ nonlinear equations (Eq. 2.72) is solved through an iterative procedure and z values are computed. The procedure is outlined in the flow chart shown in Fig. 2.6.2.

2.6.3 Pinned Configuration

The boundary conditions at the clamped end are same as floating configuration. f_{N+1} and f_{N+2} are same as floating equation and are shown in Eq. 2.78 and 2.79. Hence, the corresponding Jacobian matrix values are also same as Eq. 2.82 and 2.83.
At the touching end, deflection (z) and bending moment (z'') are zero and in terms of finite differences, they are expressed as follows.

$$f_{N+3} = z_N \tag{2.86}$$

$$f_{N+4} = -z_{N-2} + 16\, z_{N-1} - 30\, z_N + 16 z_{N+1} - z_{N+2} \tag{2.87}$$

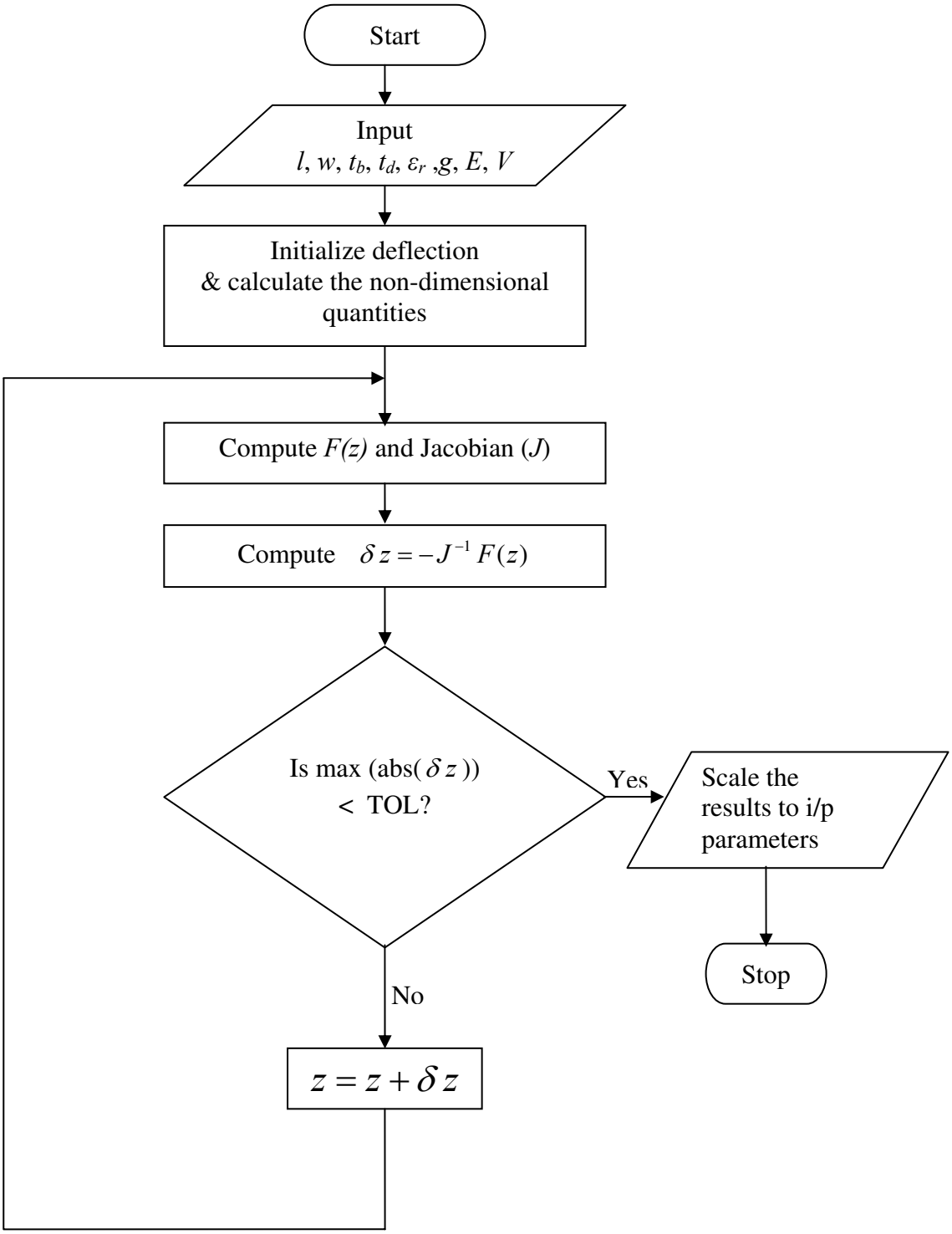

Figure 2.5: Flow chart for Finite difference approximation of floating and pinned configurations.

The corresponding Jacobian matrix elements are,

$$J_{N+3,\,N} = 1\,; \tag{2.88}$$

$$J_{N+4,\,N-2} = J_{N+4,N+2} = -1\,;\; J_{N+4,\,N-1} = J_{N+4,N+1} = 16\,;\; J_{N+4,\,N)} = -30\,; \tag{2.89}$$

The non-contact length, number of unknowns and solution procedure are exactly identical to the floating configuration as outlined in the flow chart shown in Fig. 2.6.2.

2.6.4 Flat Configuration

In this configuration, the non-contact length varies with the applied voltage and hence, is an unknown quantity. This problem turns out to be a free boundary problem. The solution procedure has a minor adition to the previous two configurations. The boundary conditions at the clamped end are same as other configurations. At the other end, deflection (z), slope (z') and bending moment (z'') are zero. Hence, unlike the other two configurations, 5 boundary conditions are known in the flat configuration.

For the flat configuration, any one solution determines all other solutions by a scaling law discussed in the following section. The procedure to find one solution, for which we assume the non-contacting length is unity, is as follows. V is initialized with an arbitrary value. The corresponding value of z is computed using the three boundary conditions at the flat end (at z_N) and zero slope condition at the fixed end (at z_1). In other words, the boundary condition that $z_1 = 1$ is initially ignored. With V given, this is enough to determine the solution. The computed value of z_1 should be unity. The chosen V is iteratively modified to match this condition. Once this V is found, all other flat solutions for the same h can be found by scaling as discussed in the following section.

The function values considered from the boundary conditions are as follows.

$$f_{N+1} = z_{-1} - 8\,z_0 + 8\,z_2 - z_3 \tag{2.90}$$

$$f_{N+2} = z_N \tag{2.91}$$

$$f_{N+3} = z_{N-2} - 8\,z_{N-1} + 8\,z_{N+1} - z_{N+2} \tag{2.92}$$

$$f_{N+4} = -z_{N-2} + 16\,z_{N-1} - 30\,z_N + 16 z_{N+1} - z_{N+2} \tag{2.93}$$

The non-zero elements of the Jacobian matrix associated with these functions are

$$J_{N+1,\,-1} = 1\,;\; J_{N+1,\,0} = -8\,;\; J_{N+1,\,2} = 8\,;\; J_{N+1,\,3} = -1\,; \tag{2.94}$$

$$J_{N+2,\,N} = 1\,; \tag{2.95}$$

$$J_{N+3,\,N-2} = 1\,;\; J_{N+3,\,N-1} = -8\,;\; J_{N+3,\,N+1} = 8\,;\; J_{N+3,\,N+2} = -1\,; \tag{2.96}$$

$$J_{N+4,\,N-2} = J_{N+4,N+2} = -1\,;\; J_{N+4,\,N-1} = J_{N+4,N+1} = 16\,;\; J_{N+4,\,N)} = -30\,; \tag{2.97}$$

2.7 Scaling Law in the Flat Configuration

In the flat regime, a scaling law is found. Due to this scaling, if the solution is computed at one voltage, solutions at all other voltages can be found out with out actually solving the governing equation again. The solution computed at one voltage can be scaled appropriately to get the solutions at all other voltages. The scaling law is deduced from the following analysis.

Let

$$\zeta = x\,\sqrt{V} \tag{2.98}$$

The governing Eq.2.10, in terms of ζ is

$$\frac{d^4 z}{d\zeta^4} = \frac{-1}{(z+h)^2} \tag{2.99}$$

Let the ζ value at $x = a$ be denoted by ζ_0. The boundary conditions expressed in terms of ζ and are

$$z(\zeta = 0) = 1 \quad and \quad z'(\zeta = 0) = 0$$

$$z(\zeta = \zeta_0) = z'(\zeta = \zeta_0) = z''(\zeta = \zeta_0) = 0 \tag{2.100}$$

It is evident from Eq. 2.99 and 2.100 that neither the governing equation nor the boundary conditions are dependent on the applied voltage. The values of ζ_0, $z(\zeta)$ for a given voltage can be computed from the numerical procedure described previously and they are constant for a given value of h. Let α be the non-contact length of the beam for an applied voltage of V. As ζ_0 is constant for a given h,

$$\alpha\sqrt{V} = \zeta_0 = constant \tag{2.101}$$

Hence, ζ_0 computed at any voltage determines the constant value and can be subsequently used to compute the non-contact lengths at all other voltages. Similarly, z value computed at one voltage can be used to compute the z values at all other voltages. Another point to be noted is that this scaling law is applicable even to the models [7, 23] that account for fringing field.

2.8 Discussion and Conclusions

Cantilever beam MEMS electrostatic actuators with an intermediate dielectric layer or modeled over the entire operational range. Three possible static configurations are identified in the operational range: floating, pinned and flat configurations. The non-contact length in all the configurations is governed by the same equation but they differ in the boundary conditions. Modal expansion method and finite difference method are developed to perform the simulations. A scaling law is found in the flat configuration. Using this scaling, solution computed at one voltage is aprropriately scaled to get the solutions at all other voltages in the flat configuration. The governing Eq. 2.10 along with the boundary conditions constitutes a nonlinear boundary value problem for the floating and

pinned configurations and a nonlinear free boundary problem for the flat configuration. The free boundary problem is transformed into an iterative boundary value problem by using the additionally available boundary condition.

Chapter 3

Effects of Dielectric Layer

3.1 Introduction

The governing Eq. 2.10 has only two parameters V and h. h is proportional to the dielectric thickness for a given zero bias height and dielectric constant. Similarly, V is proportional to the applied voltage. The effects of dielectric layer thickness are studied by finding out the solutions for fixed h and varying V, for a range of values of h.

The following section gives details regarding voltage limits of the three possible configurations of the beam.

3.2 Normalized Voltage (V) Limits of Configurations

1. *Floating Configuration*: The lower limit (V_{float}^{min}) is, trivially, zero. The upper limit (V_{float}^{max}) is decided either by disappearance of solutions via a so-called turning point (for small h, as discussed later), or (for large h) contact with the dielectric layer. Beyond this upper limit, the actuator switches to the pinned or flat configuration.

2. *Pinned Configuration*: The end of the beam can, in principle, always be held pinned (say, by an external agent) against the dielectric layer by a suitable additional vertical force at the end point. If that force needs to act downwards, then such a pinned solution is physically unfeasible because when we remove that force the

end point moves up. Upward acting forces are feasible because when we remove that force the end point tends to move down and presses against the dielectric layer which, through mechanical contact, can apply an upward force.

The lower limit (V_{pin}^{min}) is therefore voltage at which shear force at the contacting end of the cantilever beam becomes zero (and the boundary conditions of the pinned configuration are also satisfied). Below V_{pin}^{min}, the dielectric layer would have to *mechanically* pull down on the free end: since it cannot do so, the actuator is in the floating configuration. The upper limit (V_{pin}^{max}) is decided either by disappearance of solutions via a so-called turning point (for small h, as discussed later), or (for large h) extended contact with the dielectric layer (zero slope at the end). Beyond this upper limit, the actuator switches to the flat configuration. The transition at (V_{pin}^{max}) has not been elucidated in the literature, and is one of post-pull-in insights offered in this thesis.

3. *Flat configuration*: The lower limit (V_{flat}^{min}) is that at which the non-contacting length of the beam equals the total length of the beam. There is no upper V limit for the flat configuration. The non-contacting length approaches zero as $V \to \infty$.

V limits for the three configurations, computed for varying h values, are shown in Fig. 3.1. Possible transitions between configurations are shown in Fig. 3.2, based on Fig. 3.1.

3.3 Transitions

Four transitions are identified, as suggested by Fig. 3.2. The following insights into transitions from one configuration to another would be impossible with lumped parameter models, and somewhat obscured with 3-D models. These simple insights form one of the main benefits of the beam model for the actuator.

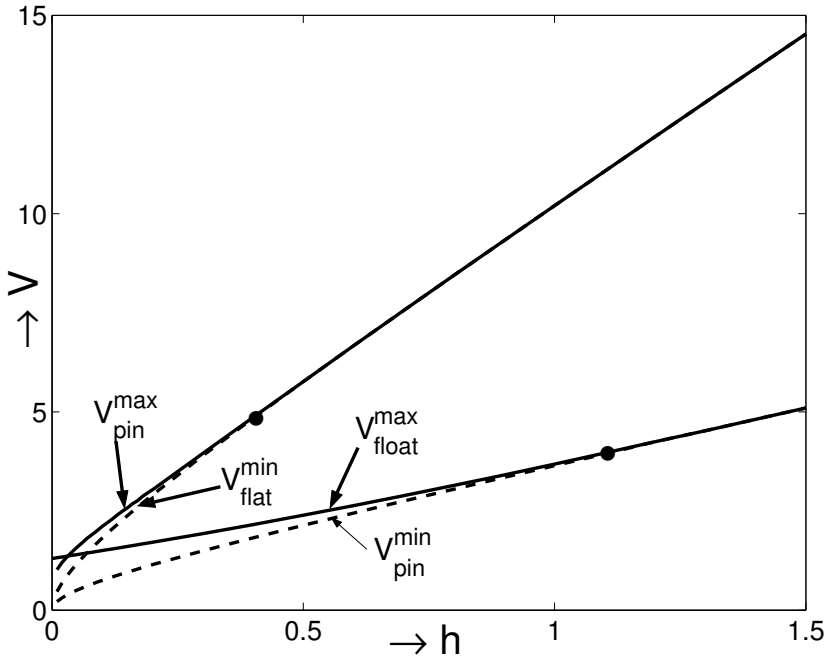

Figure 3.1: V limits of the three configurations.

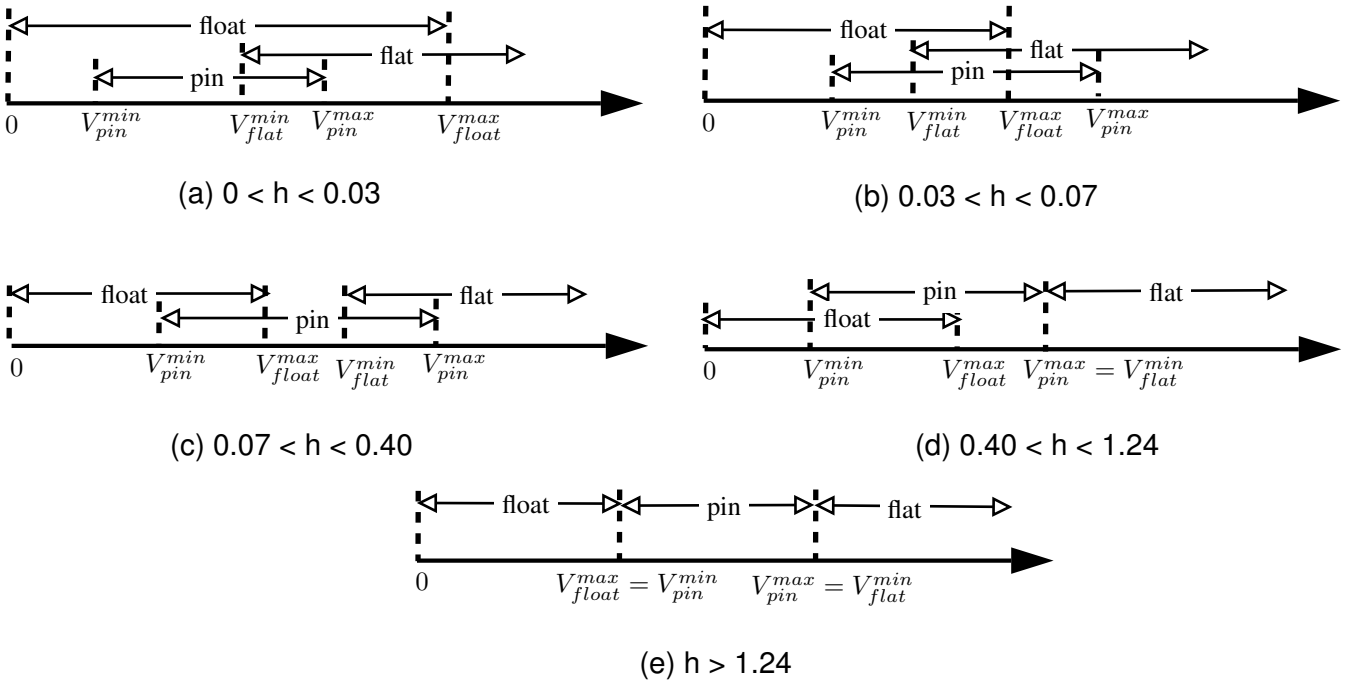

Figure 3.2: Classification of possible transitions based on the numerical results of Fig. 3.1.

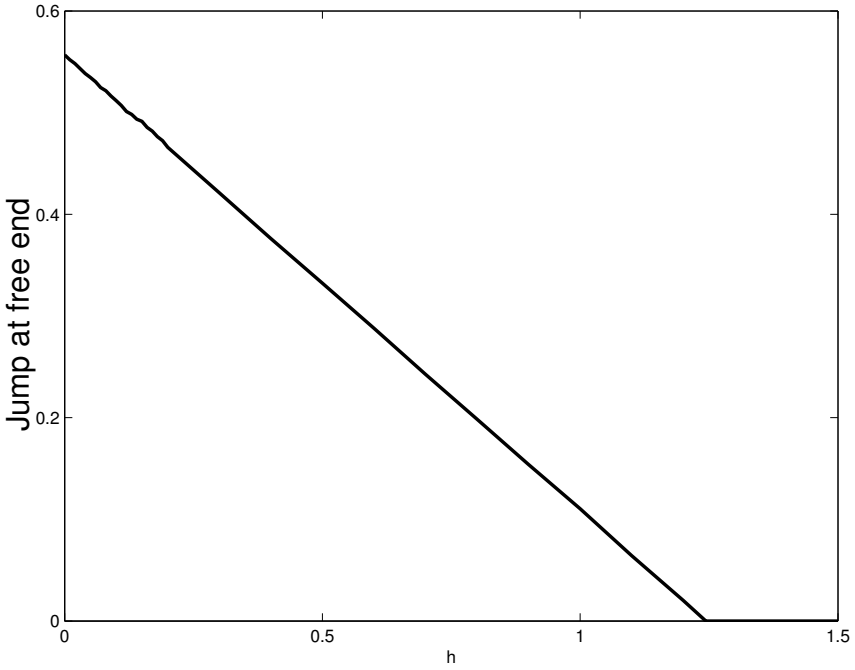

Figure 3.3: Variation of the magnitude of the pull-in discontinuity with h.

3.3.1 Pull-In

Pull-in occurs when the floating configuration solution disappears, as discussed earlier. Figure 3.3 shows the magnitude of the pull-in discontinuity for varying h values. The jump in the height at the free end of the beam at the point of transition results from a turning point bifurcation, as discussed later. Here, we note (Fig. 3.3) that the magnitude decreases essentially linearly with increasing h. It is interesting to note that for $h < 0.03$ (Fig. 3.2(a)), the transition from floating has to be to the flat configuration. For $0.03 < h < 0.07$ (Fig. 3.2(b)), the transition could be to either the pinned or the flat configuration, and only a full nonlinear dynamic analysis (not attempted here) can resolve which configuration is reached immediately after pull-in. For $h > 0.07$, the transition has to be to the pinned configuration. Upon increasing the voltage, regardless of h, any pinned configuration will transition to a flat configuration.

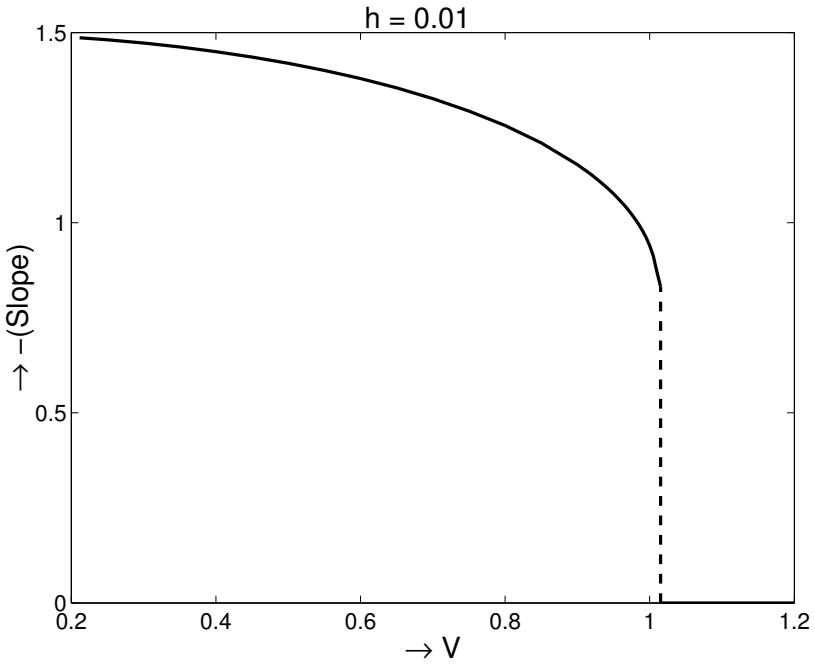

Figure 3.4: Pull-down: jump in slope at the touching end of the beam.

3.3.2 Pull-Down

The transition from the pinned to the flat configuration is referred to here as *pull-down*. The pinned configuration has a nonzero slope at the beam's end point, while the flat configuration has zero slope. As is the case for pull-in, a discontinuous transition from pinned to flat occurs due to a turning point bifurcation, as discussed later. Figure 3.4 shows the pull-down discontinuity decreases faster and faster, until the curve turns around (not shown here; see discussion later) and the pinned solution disappears. Figure 3.5 shows the magnitude of the pull-down slope discontinuity for different h. For $h > 0.4$, the discontinuity in the transition disappears.

3.3.3 Pull-Up

Starting in the flat configuration, a transition is possible to a pinned configuration. Here, we refer to such a transition as pull-up. Again, for $h > 0.4$, pull-up is continuous (Fig. 3.2).

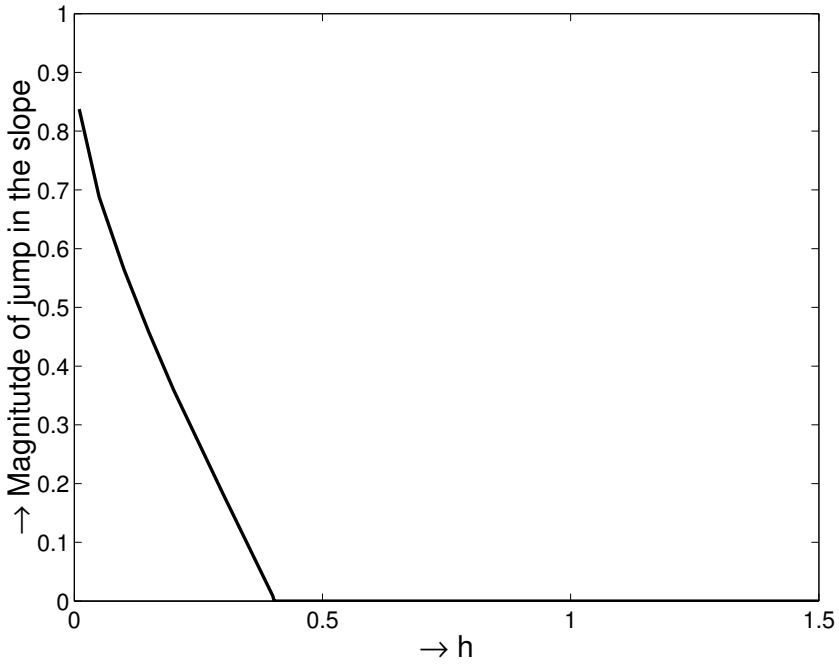

Figure 3.5: Variation of the magnitude of the pull-down discontinuity with h.

In addition, for $h < 0.07$, it is not clear without nonlinear dynamics analysis (not conducted here) whether the transition at V_{flat}^{min} occurs to the pinned or the floating configuration. Note that any pinned configuration must eventually transition to the floating configuration as V is decreased.

3.3.4 Pull-out

Finally, the transition from either pinned or flat to floating is called pull-out. Note that, as is widely observed in experiments, pull-out does not in general occur at the same voltage as pull-in; however, for large enough h, it does. This consistency in physical behaviour may be useful in applications.

3.4 Bi-stability

It can be seen from Fig. 3.2 that below a certain value of h, there is a overlap between the voltage ranges of two different configurations. It means that the actuator has two stable

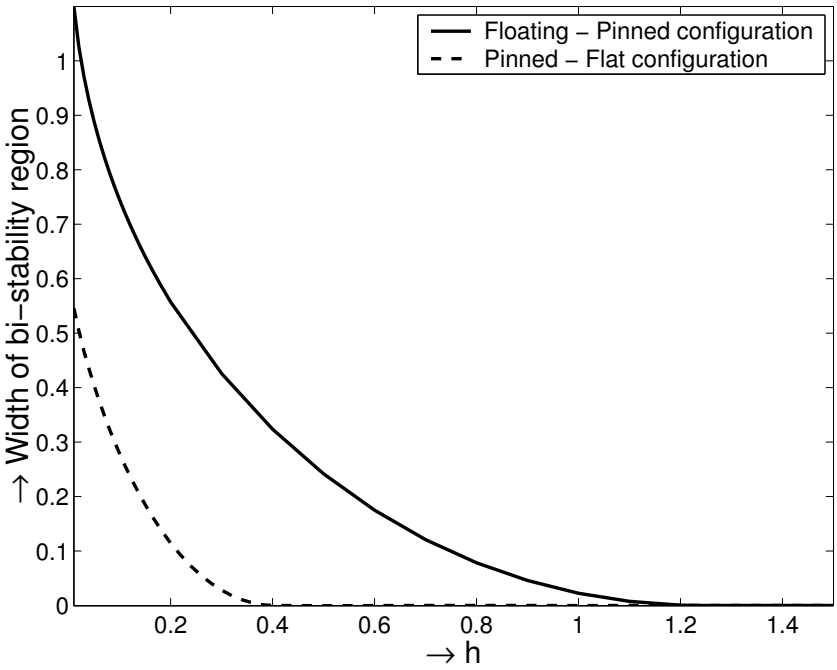

Figure 3.6: Variation of width of bi-stability region with h.

solutions in the overlap region and it can stay in either of the states. This is known as *hysteresis* or *bi-stability*.

The width of bi-stability regions between the floating-pinned and the pinned-flat configurations, as a function of h, is shown in Fig. 3.6. Bi-stability between the pinned and flat configurations disappears for $h > 0.4$. Similarly, there is no bi-stability between floating and pinned configurations for $h > 1.24$.

Note that for $h < 0.07$, there are three stable states for certain values of V. Therefore, there is a *tri*-stability for $h < 0.07$. The existence of tri-stable states has not previously been noted for such actuators in the literature.

3.5 Discussion and Conclusions

Voltage limits are computed for all the three possible configurations. A frame work of all possible types of transitions is made based on the overlaps in voltage ranges of these configurations. Tri-stable states are observed for the first time for very small values of h. With the increase in dielectric layer thickness, magnitude of the discontinuities and width

of bi-stability regions decreases. For $h > 1.24$, all the transitions are continuous and the bi-stable states disappear. Hence, the actuator has a smooth, predictable and reversible behaviour for larger value of h.

Chapter 4

Dynamic Stability of Equilibrium Solutions

4.1 Introduction

The governing Eq. 2.10 is nonlinear and hence, it can have multiple equilibrium solutions. The solution obtained depends on the initial guess. Some of these solutions are infeasible as they penetrate into the dielectric layer. Physically feasible equilibrium solutions may or not be dynamically stable. In this chapter, we perform the dynamic stability analysis of all the physically feasible equilibrium solutions in the floating and pinned configurations. The correlation of these results to chapter 3 is also discussed.

4.2 Method

The dynamic stability of an equilibrium solution can be determined by considering small variations of that solution, and is governed by an eigenvalue problem.

Let z_{eq} be an equilibrium solution. Then

$$\frac{\partial^4 z_{eq}}{\partial x^4} = -\frac{V^2}{(z_{eq}+h)^2} \tag{4.1}$$

Let ζ be a small perturbation to z_{eq}. Putting

$$z = z_{eq} + \zeta \tag{4.2}$$

in Eq. 2.9,

$$\frac{\partial^4 (z_{eq} + \zeta)}{\partial x^4} + \frac{\partial^2 (z_{eq} + \zeta)}{\partial t^2} = -\frac{V^2}{(z_{eq} + \zeta + h)^2}.$$

Linearizing for small ζ using Taylor series expansion,

$$\frac{\partial^4 (z_{eq} + \zeta)}{\partial x^4} + \frac{\partial^2 (z_{eq} + \zeta)}{\partial t^2} = -\frac{V^2}{(z_{eq} + h)^2} + \frac{2V^2}{(z_{eq} + h)^3}\,\zeta. \tag{4.3}$$

By Eq. 4.1,

$$\frac{\partial^4 \zeta}{\partial x^4} + \frac{\partial^2 \zeta}{\partial t^2} = \frac{2\,V^2}{(z_{eq} + h)^3}\,\zeta. \tag{4.4}$$

The above system is discretized using modal expansion [31] along the lines of chapter 2.5, by letting

$$\zeta(x,\, t) = \sum_{i=1}^{n} a_i(t)\, \psi_i(x) \tag{4.5}$$

where $\psi_i(x)$ is the i^{th} normal (or natural) mode of the beam in the absence of electrostatic forces, and $a_i(t)$ is the associated modal coordinate or participation factor. Large n gives high accuracy. The normal modes used are

$$\psi_i(x) = \cosh(\lambda_i\, x) - \cos(\lambda_i\, x) - B_i\,(\sinh(\lambda_i\, x) - \sin(\lambda_i\, x))\,. \tag{4.6}$$

We have the following results from the derivations in chapter 2.5.

1. *Floating*:

   λ_i is the i^{th} root of

   $$1 + \cosh(\lambda_i)\ \cos(\lambda_i) = 0 \tag{4.7}$$

   and

   $$B_i = \frac{\sinh(\lambda_i) - \sin(\lambda_i)}{\cosh(\lambda_i) + \cos(\lambda_i)}. \tag{4.8}$$

2. *Pinned*:

   λ_i is the i^{th} root of

$$\coth(\lambda_i) - \cot(\lambda_i) = 0 \tag{4.9}$$

   and

$$B_i = \coth(\lambda_i). \tag{4.10}$$

Stability analysis of the flat configuration is more difficult because the contacting length of the beam changes during motion. Such an analysis is not attempted here. Note, however, that an extended contact region suggests, intuitively, that the flat configuration is stable.

The normal modes are, as the name suggests, orthonormal:

$$\int_0^1 \psi_i(x)\psi_j(x)\,dx = \begin{cases} 1 & \text{if } i = j, \\ 0 & \text{otherwise.} \end{cases} \tag{4.11}$$

From Eq. 4.6,

$$\frac{\partial^4 \psi_i(x)}{\partial x^4} = \lambda_i^4 \psi_i(x) \tag{4.12}$$

Equation 4.4 becomes

$$\sum_{i=1}^{n} \left[\frac{\partial^2 a_i(t)}{\partial t^2}\,\psi_i(x) + \lambda_i^4\, a_i(t)\,\psi_i(x) \right] \approx \frac{2\,V^2}{(z_{eq}+h)^3} \sum_{i=1}^{n} a_i(t)\,\psi_i(x), \tag{4.13}$$

where we write "$\approx$" instead of "$=$" to emphasize that a finite-n approximation is being made.

Multiplying the above with $\psi_j(x)$, $j = 1, 2, \cdots, n$, and integrating over the length, we obtain

$$\frac{\partial^2 a_j(t)}{\partial t^2} + \lambda_j^4\, a_j(t) = \sum_{i=1}^{n} a_i(t) \int_0^1 \frac{2\,V^2}{(z_{eq}+h)^3}\,\psi_i(x)\,\psi_j(x)\,dx, \tag{4.14}$$

where we have reintroduced "$=$" instead of "$\approx$" for convenience, although the finite-n approximation remains. Note, also, that the integral on the right hand side requires knowledge of $z_{eq}(x)$ from a separate calculation.

In matrix form,

$$\frac{\partial^2 \vec{a}}{\partial t^2} + \Lambda^4 \, \vec{a} - B \, \vec{a} = 0 \tag{4.15}$$

where

$$\vec{a} = [\, a_1(t), \;\; a_2(t), \;\; a_3(t), \;\; \cdots\cdots \;\; a_n(t) \,]^T \tag{4.16}$$

and Λ is a diagonal matrix with $\Lambda_{jj} = \lambda_j$. Also, B is a square matrix with

$$B_{ij} = \int_0^1 \frac{2\,V^2}{(z_{eq} + h)^3} \, \psi_i(x) \, \psi_j(x) \, dx. \tag{4.17}$$

Let $\vec{a} = \vec{u} \; e^{\sigma t}$. Substituting in Eq. 4.15,

$$\left(-\Lambda^4 + B\right) \vec{u} = \sigma^2 \; \vec{u}. \tag{4.18}$$

The eigenvalues of the above system determine stability. By the symmetry of Λ and B, all σ^2 are real. If all σ^2 are *negative*, then all solutions are linear combinations of sinusoidal oscillations; and the original equilibrium solution is dynamically stable. A positive σ^2 implies instability. At a stability boundary, one eigenvalue will be $\sigma^2 = 0$ (a degenerate case).

Rigorous analysts will note that such stability only holds within the linear approximation and is neutral at best; deeper analysis is required, in principle and for general problems, to resolve rigorously whether small perturbations or nonlinearities or errors from finite n can actually make the system unstable. However, experience with vibrations of other conservative systems in engineering suggests that the stability condition used here is reliable. The results obtained below are also intuitively acceptable. In any case, an equilibrium solution found to be *unstable* by this method certainly is much more unstable than any weak instabilities that might conceivably exist in the solutions found to be stable by the truncated (finite-n) linear analysis. Thus, this analysis acts as a reliable discriminator between strongly unstable solutions and solutions that are probably stable but failing that are, at most, very weakly unstable.

Note that the numerical integration to be performed in Eq. 4.17 requires z_{eq} and ψ values at the mesh points. Of these, z_{eq} was computed above at a number of mesh points; and ψ was given above. All integrations were performed using Simpson's rule. Three normal modes were used in the stability analysis.

4.3 Stability Results

Figures 4.1 and 4.2 show the results of stability analysis for the floating and pinned configurations respectively. Each point on each curve represents an equilibrium solution (floating or pinned). Solid lines indicate stable, and dashed lines unstable solutions. Where the two branches coalesce in a turning point, the solution is borderline unstable by linear analysis. The value of V at the turning point represents pull-in and pull-down in the floating and pinned configurations respectively.

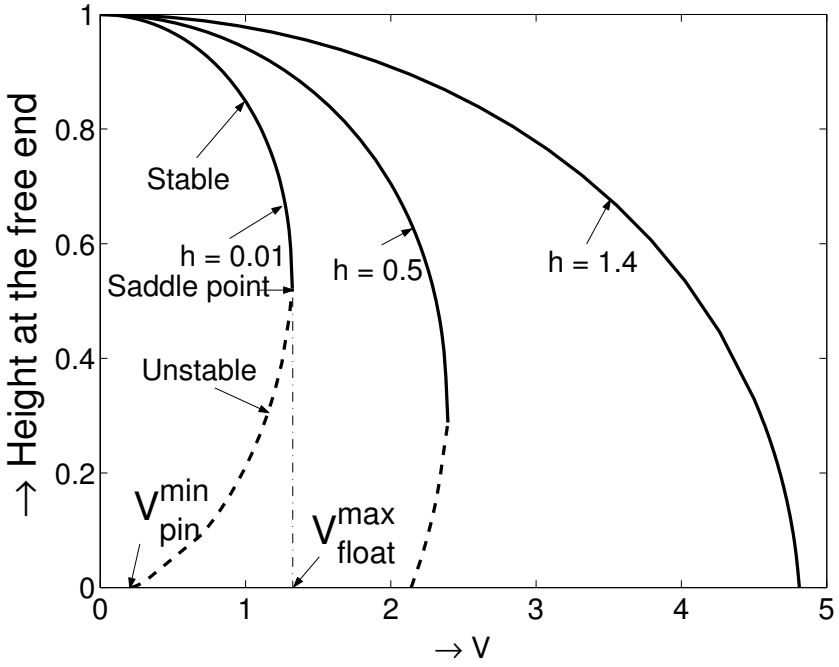

Figure 4.1: Stability analysis of the floating configuration.

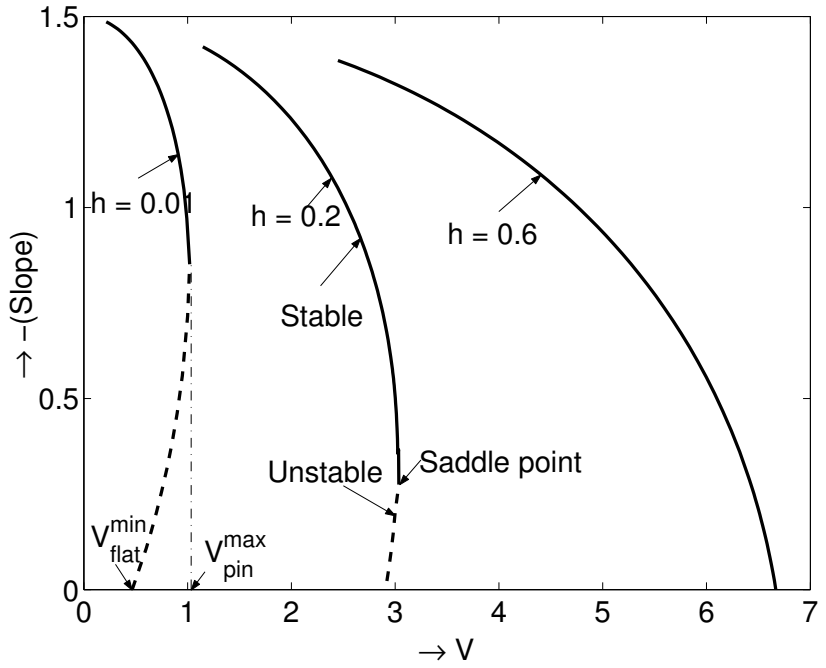

Figure 4.2: Stability analysis of the pinned configuration.

4.4 Discussion and Conclusions

The stability results plotted above also include families of equilibrium solutions plotted therein. It is useful to discuss these plots in light of chapter 3.

1. In Fig. 4.1, turning points indicate V_{float}^{max}. If there are no turning points (large h), intersection with the horizontal axis indicates V_{float}^{max}. Whether a turning point exists or not, intersection with the horizontal axis always indicates a floating solution where the beam tip just contacts the dielectric surface; the same solution happens to be a pinned solution as well, with the contact force equal to zero. The corresponding V is therefore V_{pin}^{min} (recall discussion of chapter 3.2).

   The above result, though probably not new, is apparently not well known in the MEMS community. We discuss it further, briefly, from a mechanical point of view. If there is no turning point in the curve, then the slope of the curve is negative; this means decreasing V tends to raise the beam tip off the dielectric surface, following a stable solution curve. Thus, reducing V causes disappearance of the pinned solution. Conversely, increasing V would tend to lower the beam tip into the dielectric

surface, bringing a vertical contact force into play and producing a pinned solution. Hence, the intersection marks V_{pin}^{min}.

On the other hand, if there is a turning point, then slightly raising V produces a floating solution where the beam tip is slightly above the dielectric surface. However, that solution is *unstable*, and so a slight downward perturbation to it will cause the beam tip to come down further until it touches the dielectric surface, producing a pinned solution. Conversely, lowering V slightly would make the beam tip tend to dip below the dielectric surface; this would bring into play an upward acting contact force, disturbing the solution; and, the solution being unstable, would make the beam move further up, away from the pinned state.

In this way, simultaneous consideration of equilibrium and stability helps us understand why the intersection point of the floating solution curve with the horizontal axis indicates V_{pin}^{min}.

2. Similarly, considering the pinned configuration illustrated in Fig. 4.2 (the vertical axis shows the slope at the end of the beam), we observe that V_{pin}^{max} is the maximum V at which a stable solution exists (whether there is a turning point or not), and the solution curve intersects the horizontal-axis at V_{flat}^{min}.

3. For $h > 0.4$, all pinned solutions are stable. In other words, $V_{pin}^{max} = V_{flat}^{min}$. Simultaneously stable pinned and flat solutions no longer coexist (this mode of bi-stability disappears).

4. For $h > 1.24$, all floating solutions are stable, and $V_{float}^{max} = V_{pin}^{min}$. Simultaneous multiple stable solutions of any kind no longer exist.

Chapter 5

Case Study

The analysis carried out so far was in terms of normalized, non-dimensional quantities. Such analysis, though broadly applicable, need to be recast or reinterpreted in terms of actual lengths, voltages, and material properties for developing insight into specific physical applications. With this view, in this chapter, typical dimensions of a MEMS actuator are assumed and the foregoing results are cast in terms of physical variables.

The dimensions and material properties considered are shown in Table 5.1. These parameters correspond to $h = 0.1$.

Figure 5.1 shows the variation of height at the free end of the beam with applied voltage. Pull-in occurs at 1.46 V and there is a jump in the height of the free end from $0.96\,\mu$m to $0\,\mu m$. Stability analysis shows, as expected, that equilibrium solutions with end point heights below $0.96\,\mu$ m (represented by a dashed line) are dynamically unstable. The solution space intersects the horizontal axis at 0.73 V.

Table 5.1: Dimensions and material properties of a MEMS actuator.

Parameter	Value
Plate dimensions	400×100 μm^2
Plate thickness	1 μm
Zero bias gap	2 μm
Young's modulus	160 GPa
Dielectric material	Si_3N_4
Dielectric constant	7
Dielectric thickness	1.4 μm

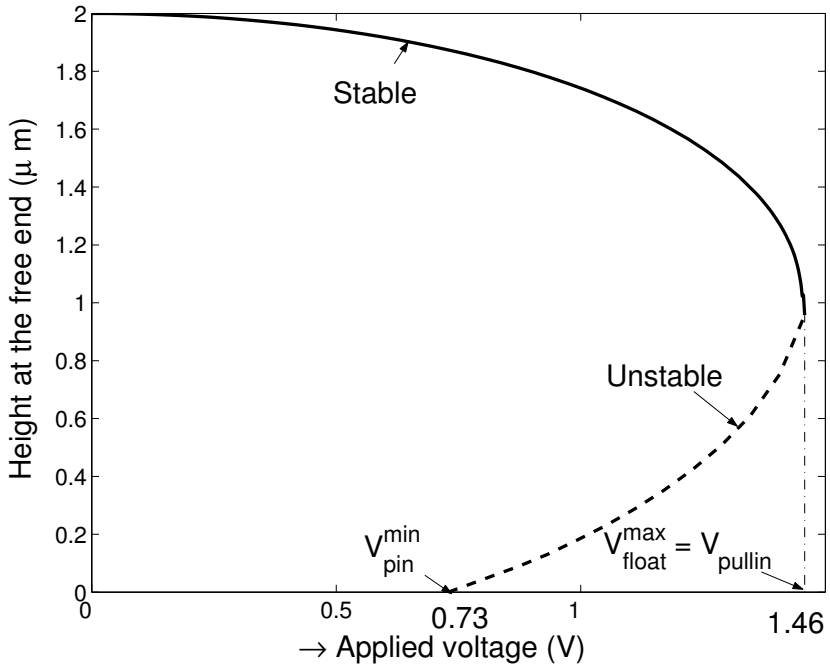

Figure 5.1: Floating configuration: Variation of height at the free end of the beam with applied voltage.

Figure 5.2 shows the force at the contact point of the cantilever beam vs. applied voltage for the pinned beam boundary conditions. The sign convention is that negative values indicate an upward mechanical contact force acting from the dielectric on the end point of the beam. At 0.73 V, the contact force is zero, corresponding to V_{pin}^{min} as discussed above. This voltage matches, as it must, the voltage at which the floating solution curve intersects the x-axis. Figure 5.3 shows the variation of slope at the contact point with the applied voltage. Pull-down occurs at 2.05 V and the slope at the contact point jumps from -2.99×10^{-3} to 0. Note that this (non-dimensional) slope is small compared to unity, showing *post facto* that the linear behaviour assumed in the beam mechanics (as opposed to the electrostatic loading) is valid.

Solutions with contact point slope below -2.99×10^{-3} (represented by a dashed line) are unstable. The solution space intersects the x-axis at 1.76 V.

Figure 5.4 shows the variation of the contact length of the cantilever beam vs. applied voltage in the flat configuration. V_{flat}^{min} from the figure is 1.76 V. As discussed above, this voltage matches the voltage at which the pinned solution curve intersects the horizontal

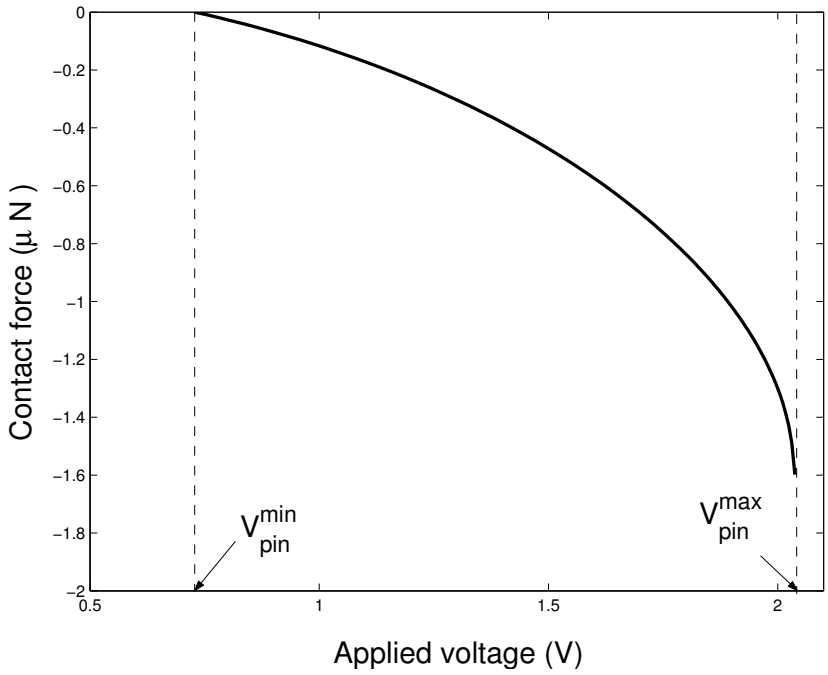

Figure 5.2: Pinned configuration: Contact force at the touching end of the beam vs. applied voltage.

axis. Figure 5.5 summarizes the voltage ranges of all the three configurations.

Figure 5.6 shows the capacitance-voltage (C-V) characteristics of the actuator in the floating configuration. The capacitance at zero potential is 0.161 pF and at the pull-in voltage is 0.201 pF. Hence, within the restrictions of the present model, the actuator has a tunability of 25 % in the floating configuration (this proportion turns out to be only weakly dependent on dielectric layer thickness for small values thereof, because the beam tip is still far from the dielectric layer).

Maximum capacitance in the flat configuration is achieved when the upper plate completely comes in contact with the dielectric layer: this limit corresponds to $V = \infty$ and a breakdown of the beam theory assumptions made in the model. We will retreat from this limit later; but for now, we write

$$C_{max} = \frac{\epsilon_0 \, \epsilon_r \, w \, l}{t_d}. \tag{5.1}$$

For the parameter values used here, $C_{max} = 1.771$ pF. Let C^* denote the capacitance for

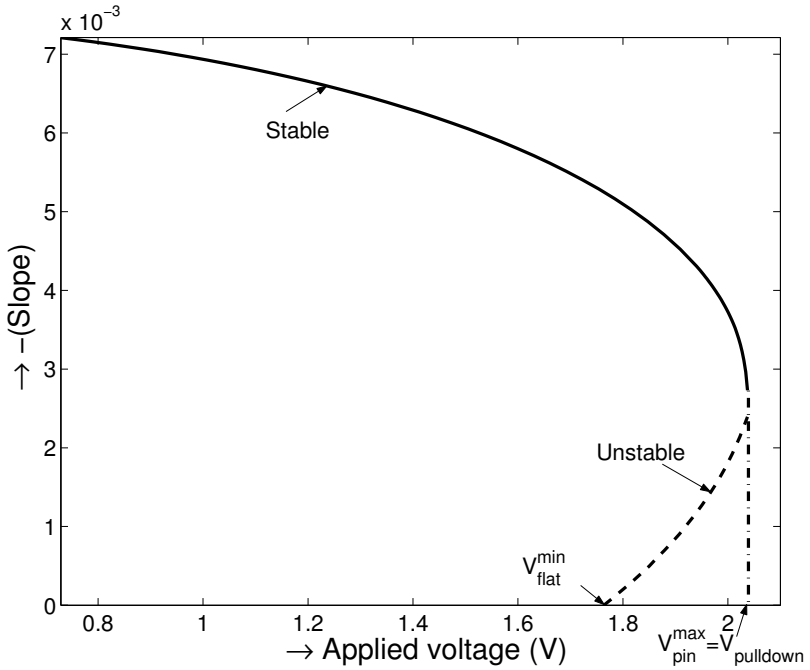

Figure 5.3: Pinned configuration: Slope at the contact point of the cantilever beam vs. applied voltage.

a non-contact length of l in the flat configuration and let the corresponding voltage be V^*. For the parameter values used here, $C^* = 0.621$ pF and $V^* = 1.76$ V.

For an arbitrary applied voltage V in the flat regime, let the non-contact length and the capacitance be a and C respectively.Then

$$C = \frac{a}{l} C^* + \frac{\epsilon_0 \, \epsilon_r \, w \, (l - a)}{t_d}. \tag{5.2}$$

Fig. 5.7 shows the C-V characteristics when the minimum non-contact length is limited to 20 % of the total length of the beam. The voltage range considered is 2.05 – 44 V to ensure that we stay within the same (flat) configuration. The capacitance range is 0.705 – 1.541 pF, with a tunability of 120 %. Thus, the actuator offers larger tunability in the flat configuration than in the conventional floating configuration. Unlike in the floating configuration, the maximum variation in capacitance occurs in the initial part of the applied voltage range.

We end this chapter with a few qualitative observations. Low dielectric thickness gives

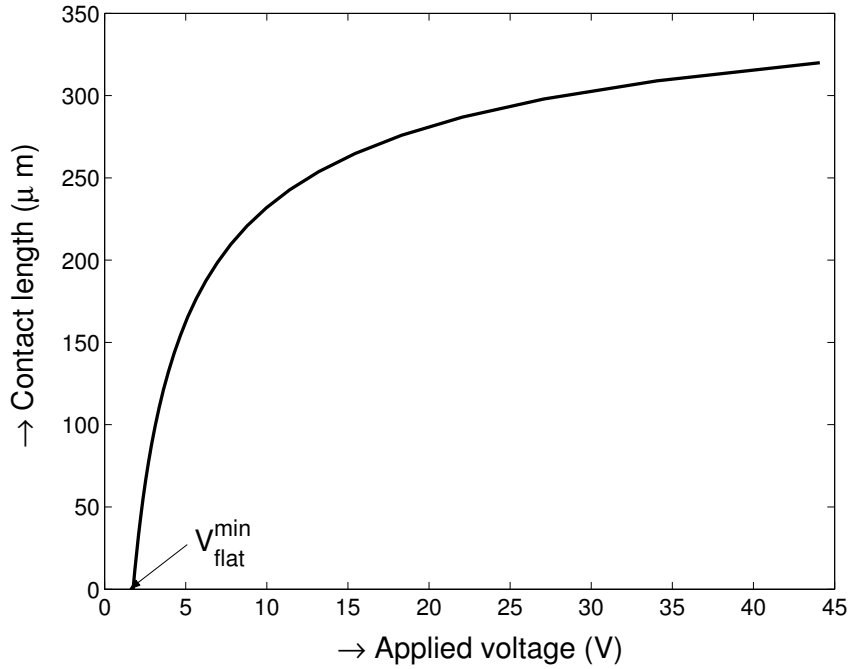

Figure 5.4: Flat configuration: Contact length of the cantilever beam with the dielectric layer vs. applied voltage.

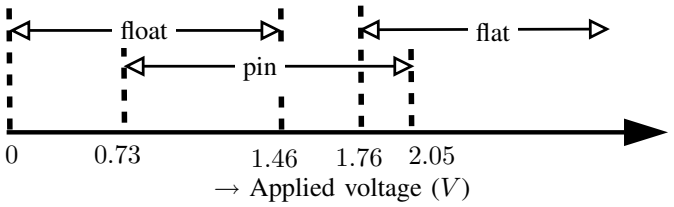

Figure 5.5: Voltage ranges of the three configurations.

greater tunability, but at the cost of discontinuous transitions, multiple coexisting stable states, and hence less predictable behaviour. These problems can be eliminated with a high dielectric thickness *near the beam tip*. However, lower dielectric thickness away from the beam tip will not cause such problems, while increasing the tunability. In this way, we anticipate that a dielectric layer of suitably varying thickness may give a large operational voltage range with both predictable behaviour as well as high tunability.

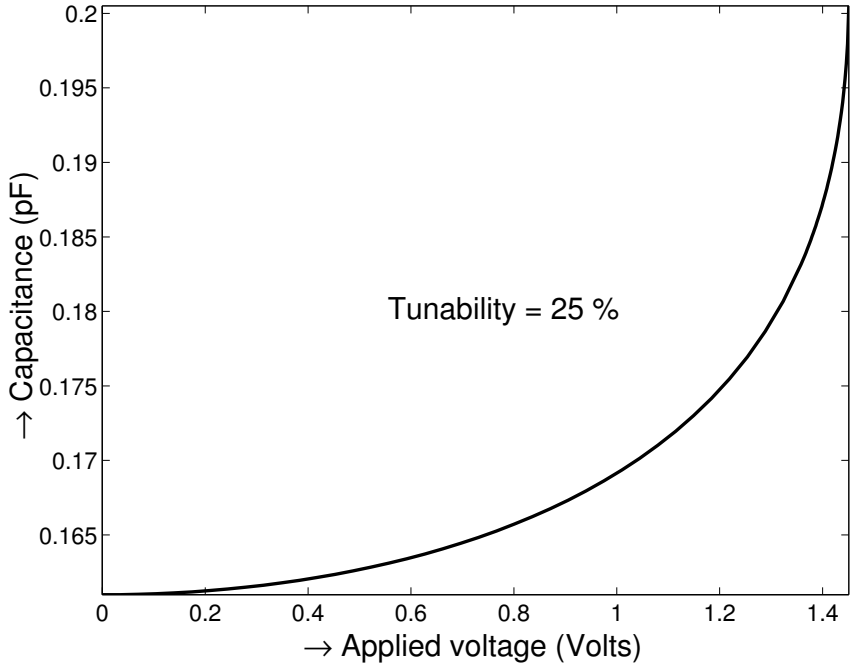

Figure 5.6: C-V characteristics in the floating configuration.

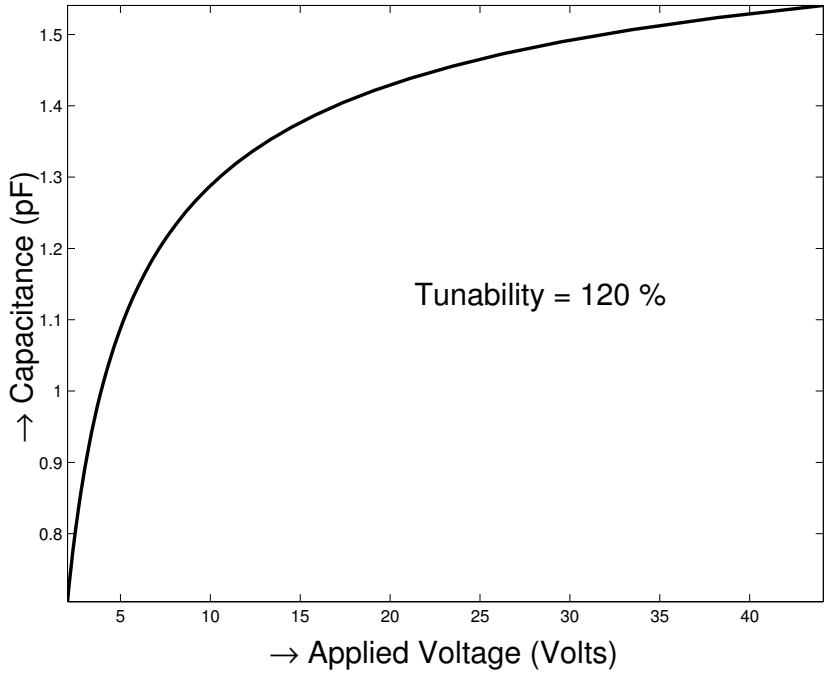

Figure 5.7: C-V characteristics in the flat configuration.

Chapter 6

Conclusions and Further Work

Cantilever beam electrostatic actuators with an intermediate dielectric layer have been analyzed in detail over the entire operational range using a beam model.

Three qualitatively different configurations, here called floating, pinned and flat, have been identified and studied. A scaling law is found in the flat configuration. Transitions from and to the floating configuration (pull-in and pull-out) and transitions from pinned to flat (pull-down) and flat to pinned (pull-up) have been studied as well. Bi-stable and tri-stable states have been found. A classification of all possible types of transitions is made based on the dielectric layer parameters. Dynamic stability analyses have complemented the study of these configurations and transitions.

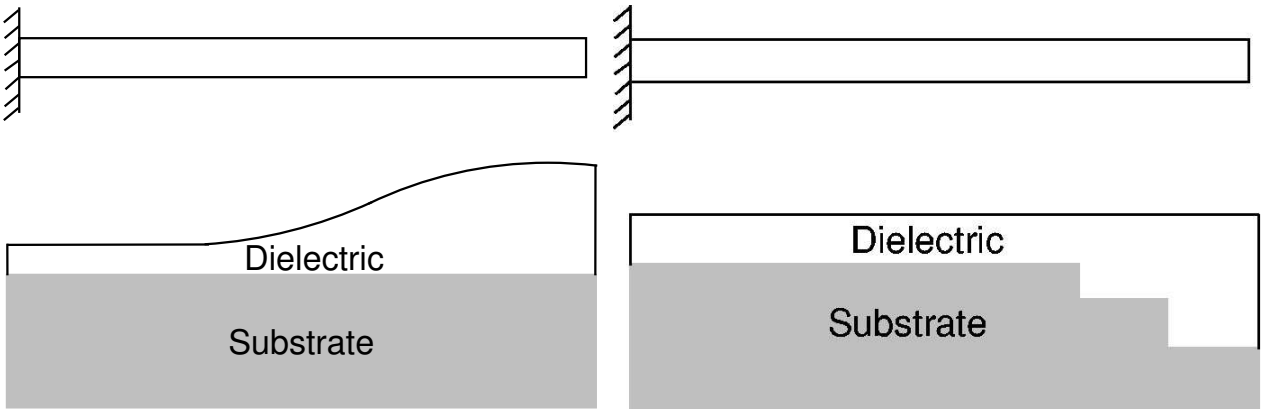

Figure 6.1: Proposed designs to achieve more regular and reversible behaviour as well as higher tunability

Higher dielectric thickness gives more regular and predictable behaviour, at the cost of lower overall tunability in device characteristics. Hence, designs similar to Fig. 6.1, with higher dielectric thickness near the free end may result in more regular and reversible behaviour as well as higher tunability. In the first proposed design, the dielectric thickness is low over most of the beam and is smoothly increasing to a significantly larger value near the free end. In the second design, the thickness of the substrate is decreased in steps near the right end and a dielectric layer is deposited over the substrate with its outer surface being at a constant height. Such designs may also be useful in achieving the desired C-V characteristics.

In future works, behaviour of MEMS actuators with varying dielectric thickness can be studied in detail. Similar analysis can be carried out for fixed-fixed and circularly clamped MEMS electrostatic actuators.

Bibliography

[1] L. A. Rocha, E. Cretu, and R. F. Wolffenbuttel, "Full characterisation of pull-in in single-sided clamped beams," *Sensors Actuators A*, vol. 110, pp. 301–309, Feb. 2004.

[2] V. Shrivastava, N. R. Aluru, and S. Mukherjee, "Numerical analysis of 3D electrostatics of deformable conductors using a Lagrangian approach," *Engineering Analysis with Boundary Elements*, vol. 28, no. 6, pp. 583–591, June 2004.

[3] M. I. Younis, E. M. Abdel-Rahman, and A. H. Nayfeh, "A reduced-order model for electrically actuated microbeam-based MEMS," *IEEE J. Microelectromechanical Systems*, vol. 12, no. 5, pp. 672–680, Oct. 2003.

[4] E. M. Abdel-Rahman, M. I. Younis, and A. H. Nayfeh, "Characterization of the mechanical behavior of an electrostatically actuated microbeam," *J. Micromech. Microeng.*, vol. 12, no. 6, pp. 759–766, Nov. 2002.

[5] S. D. Senturia, *Microsystem Design.* Boston, MA: Kulwer Academic, 2001.

[6] G. M. Rebeiz, *RF MEMS: Theory, Design and Technology.* New Jersey: John Wiley and Sons, 2003.

[7] R. K. Gupta, "Electrostatic Pull-In test structure design for in-situ mechanical property measurements of microelectromechanical systems (MEMS)," Ph.D. dissertation, MIT, June 1997.

[8] E. S. Hung and S. D. Senturia, "Generating efficient dynamic models for microelectromechanical systems from a few finite element simulation runs," *IEEE J. Microelectromechanical Systems*, vol. 8, no. 3, pp. 280–289, Sep. 1999.

[9] L. D. Gabby, J. E. Mehner, and S. D. Senturia, "Computer-aided generation of reduced-order dynamic macromodels-I: Non-stress-stiffened case," *IEEE J. Microelectromechanical Systems*, vol. 9, no. 2, pp. 262–269, June 2000.

[10] S. D. Senturia, "CAD challenges for microsensors, microactuators and microsystems," in *Proc. IEEE*, vol. 86, Aug. 1998, pp. 1611–1626.

[11] J. A. Pelesko, "Mathematical modeling of electrostatic MEMS with tailored dielectric properties," *SIAM J. Appl. Math.*, vol. 62, no. 3, pp. 888 – 908, Jan. 2002.

[12] C. Goldsmith, J. Randall, S. Eshelman, T. H. Lin, D. Denniston, S. Chen, and B. Norvell, "Characteristics of micromachined switches at microwave frequencies," in *IEEE MTT-S International Microwave Symposium Digest*, vol. 2, San Francisco, June 1996, pp. 1141–1144.

[13] J. B. Muldavin and G. M. Rebeiz, "High-isolation CPW MEMS shunt switches. 1. Modeling," *IEEE Trans. Microwave Theory Tech.*, vol. 48, no. 6, pp. 1045 – 1052, June 2000.

[14] E. S. Hung and S. D. Senturia, "Tunable capacitors with programmable capacitance-voltage characteristic," in *Solid-State Sensors and Actuators Workshop*, June 1998, pp. 292–295.

[15] G. V. Ionis, A. Dec, and K. Suyama, "A zipper-action differential micro-mechanical tunable capacitor," in *Proceedings of MEMS Conference*, Aug. 2001, pp. 24–26.

[16] T. Ketterl, T. Weller, and D. Fries, "A micromachined tunable CPW resonator," in *IEEE MTT-S International Microwave Symposium Digest*, vol. 1, Phoenix, AZ, May 2001, pp. 345–348.

[17] H. C. Nathanson, W. E. Newell, R. Wickstrom, and J. R. Davis, "The resonant gate transistor," *IEEE Transactions on Electron Devices*, vol. ED-14, no. 3, pp. 117–133, Mar. 1967.

[18] H. A. C. Tilmans, "Equivalent circuit representation of electromechanical transducers: I. lumped-parameter systems," *J. Micromech. Microeng.*, vol. 6, no. 1, pp. 157–176, Mar. 1996.

[19] A. Dec and K. Suyama, "Micromachined electro-mechanically tunable capacitors and their applications to RF IC's," *IEEE Trans. Microwave Theory Tech.*, vol. 46, no. 12, pp. 2587–2596, Dec. 1998.

[20] S. Pamidighantam, R. Puers, K. Baert, and H. A. C. Tilmans, "Pull-in voltage analysis of electrostatically actuated beam structures with fixed-fixed and fixed-free end conditions," *J. Micromech. Microeng.*, vol. 12, no. 4, pp. 458–464, July 2002.

[21] J. R. Gilbert, R. Legtenberg, and S. D. Senturia, "3D coupled electromechanics for MEMS: Applications of CoSolve-EM," in *Proc. of the Int. Conf. on MEMS*, Amsterdam, The Netherlands, 1995, pp. 122–127.

[22] J. R. Gilbert, G. K. Ananthasuresh, and S. D. Senturia, "3D modeling of contact problems and hysteresis in coupled electro-mechanics," in *Proc. of Ninth Int. Workshop on Microelectromechanical Systems*, Feb. 1996, pp. 127–132.

[23] E. K. Chan, K. Garikipati, and R. W. Dutton, "Characterization of contact electromechanics through capacitance-voltage measurements and simulations," *IEEE J. Microelectromechanical Systems*, vol. 8, no. 2, pp. 208–217, June 1999.

[24] E. K. L. Chan, "Characterization and modeling of electrostatically actuated polysilicon micromechanical devices," Ph.D. dissertation, Stanford University, Nov. 1999.

[25] M. Abramowitz and I. A. Stegun, *Handbook of Mathematical Functions with Formulas, Graphs, and Mathematical Tables.* Dover, 1972.

[26] [Online]. Available: http://mathworld.wolfram.com/CubicFormula.html

[27] G. M. Rebeiz and J. B. Muldavin, "RF MEMS switches and switch circuits," *IEEE microwave magazine*, vol. 2, no. 4, pp. 59–71, Dec. 2001.

[28] C. H. Mastrangelo and C. H. Hsu, "A simple experimental technique for the measurement of the work of adhesion of microstructures," in *Technical Digest- IEEE Solid-State Sensor and Actuator Workshop*, 1992, pp. 208–212.

[29] M. P. de Boer and T. A. Michalske, "Accurate method for determining adhesion of cantilever beams," *Journal of Applied Physics*, vol. 86, pp. 817–827, July 1999.

[30] W. H. Press, S. A. Teukolsky, W. T. Vetterling, and B. P. Flannery, *Numerical recipes in C: The art of scientific computing.* Cambridge University Press, 1992.

[31] A. H. Nayfeh and P. F. Pai, *Linear and Nonlinear Structural Mechanics.* New Jersey: Wiley-Interscience, 2004.